Journal of Alloys and Compounds 1033 (2025) 181280

Contents lists available at ScienceDirect

Journal of Alloys and Compounds

journal homepage: www.elsevier.com/locate/jalcom

Composition, microstructure and corrosion resistance of DED-LB additively manufactured Ti–6Al–4V alloy: Comparison with wrought alloy

Ingrid Milošev [a,b,*,1], Peter Rodič [a,1], Barbara Kapun [a], Denis Sačer [a], Anish Nair [c], Davorin Kramar [c], Andrej Jeromen [c], Edvard Govekar [c]

[a] Jožef Stefan Institute, Department of Physical and Organic Chemistry, Jamova c. 39, Ljubljana SI-1000, Slovenia
[b] Valdoltra Orthopaedic Hospital, Jadranska c. 31, Ankaran SI-6280, Slovenia
[c] University of Ljubljana, Faculty of Mechanical Engineering, Aškerčeva c. 6, Ljubljana SI-1000, Slovenia

ARTICLE INFO

Keywords:
Ti–6Al–4V alloy
Additive manufacturing
Directed-energy deposition by laser beam
Microstructure
Corrosion
Simulated physiological solution

ABSTRACT

The titanium alloy Ti–6Al–4 V is widely used in medical applications due to its favourable mechanical properties, biocompatibility, and excellent corrosion resistance. This study aims to study the composition, structure and electrochemical behaviour of additively manufactured Ti–6Al–4 V alloy produced by a directed-energy deposition of powder using a laser beam (DED-LB) and compare it to wrought alloy produced by conventional metallurgy. The surface morphology and composition of the chemo-mechanically polished wrought and DED-LB samples were analysed by X-ray diffraction, scanning electron microscopy coupled with energy-dispersive X-ray spectroscopy, atomic force microscopy coupled with scanning Kelvin probe force microscopy and X-ray photoelectron spectroscopy. The electrochemical behaviour was assessed using potentiodynamic polarisation and electrochemical impedance spectroscopy in three simulated physiological solutions (Hanks' balanced salt solution, NaCl, and artificial saliva) at 37 °C. Both alloys show highly protective corrosion behaviour in the tested media, confirming that DED-LB Ti–6Al–4 V is a promising alternative to conventional manufacturing methods for advanced metallurgical engineering applications. The alloys exhibit similar general chemical composition but different microstructure, with a lamellar α'-martensitic phase in the DED-LB fabricated alloy surrounded by prior β grains contrasting equiaxed α+ β structure of the wrought alloy. Differences in microstructure are related to differences in local chemical composition, which affect the course of the corrosion when polarised to high positive potentials of 6 $V_{Ag/AgCl}$.

1. Introduction

Ti–6Al–4 V, known as titanium grade 5, is an alpha-beta titanium alloy composed of 90 wt% titanium, 6 wt% aluminium, and 4 wt% vanadium. Due to its excellent strength-to-weight ratio [1], corrosion resistance, and biocompatibility [2–9], Ti–6Al–4 V alloy is a desirable material in various industries, including aerospace and, most notably, the medical sector [3,6]. Its application in medical implants and prosthetic devices is well-established due to its mechanical properties, which match those of human bone, thereby minimising the risk of stress shielding and enhancing implant longevity [5,6]. In the medical field, the alloy's ability to resist corrosion [2] and integrate well with biological tissues has made it the material of choice for permanent implants that must withstand the harsh environment of the human body [3,6]. Furthermore, its mechanical properties ensure it can endure the dynamic loads and stresses encountered during normal physiological activities [2,3].

Conventional manufacturing methods, such as forging, casting, and machining, have long been used to produce Ti–6Al–4 V components [10,11]. Depending on the thermal treatment, these processes result in well-characterised microstructures and predictable mechanical properties. On the other hand, the rise of additive manufacturing (AM) [12–14] has revolutionised the production of metal components, offering unprecedented design flexibility [13,15] and the ability to create complex geometries [15] that were previously unattainable with conventional methods [12,16].

AM fabricate components layer-by-layer [17], enabling the customisation of implants to suit individual patient needs and optimising

* Correspondence to: Jožef Stefan Institute, Department of Physical and Organic Chemistry, Jamova cesta 39, Ljubljana SI-1000, Slovenia.
E-mail address: ingrid.milosev@ijs.si (I. Milošev).
[1] Share the first authorship

https://doi.org/10.1016/j.jallcom.2025.181280
Received 14 March 2025; Received in revised form 21 May 2025; Accepted 28 May 2025
Available online 29 May 2025

component designs to enhance performance [10,18]. Despite these advantages, the transition to AM introduces new challenges, particularly in terms of controlling the microstructure [14,17,19] and mechanical properties of the alloy [14,20,21], which can differ significantly from those produced by conventional metallurgical methods due to the unique thermal conditions and rapid solidification involved in the printing process [12,13,22].

The microstructural differences between wrought and additively manufactured Ti–6Al–4 V are critical to understanding their mechanical [10,20] and corrosion properties [4,21,23]. Metallurgical processes typically result in uniform microstructures characterised by the presence of alpha (α-phase is the hexagonal close-packed (hcp)) and beta (β-phase is the body-centred cubic (bcc)) phases [11,19,24]. The α-phase is stable at lower temperatures, while the β-phase, V-rich phase, is stable at higher temperatures, and their combination contributes to the alloy's mechanical properties [11,25]. In contrast, AM processes can produce finer grains, non-equilibrium phases, and residual stresses due to rapid cooling and layer-by-layer deposition [12,13], resulting in unique microstructural features that can impact the alloy's properties [12,14,19].

Among various AM techniques [12,13,26], both power bed fusion (PBF) and directed-energy deposition (DED) methods [15,17,21,27–29] have emerged as suitable methods for producing Ti–6Al–4 V components. Among PBF methods [4,12,13,19,30], selective laser melting (SLM) or electron beam melting (EBM), the thermal energy of the laser beam or electron beam is used to melt a thin layer of a metal powder selectively. The component is fabricated layer-by-layer by spreading and selectively melting additional layers. Among DED methods, again, either a laser or an electron beam is applied to melt the locally fed metal powder and fuse it with the previously deposited layer. Compared to the PBF processes, laser-beam (LB) based DED (DED-LB) of metal powder enables the fabrication of components with complex geometries and tailored properties on a larger scale. [15,27,28]. Additionally, it enables in-situ repairs and cladding of 3D elements and the production of functionally graded materials and alloys by adjusting powder composition and deposition parameters in real-time [31–33]. DED-LB offers significant advantages, such as material versatility and high deposition rates [32,33]. However, it also presents challenges, including the need for precise process stability control to avoid defects like porosity [27] and residual stresses [34], which can adversely affect the performance of the final component [12].

Several advanced characterisation techniques have been employed to investigate the microstructural variations, such as X-ray diffraction (XRD) [35], to identify and quantify phases, offering insights into the crystallographic structure and phase transformations resulting from the AM process [12]. Scanning electron microscopy (SEM) coupled with energy-dispersive X-ray spectroscopy (EDS) provides high-resolution images and elemental composition maps, revealing surface morphology, grain structure, and potential defects such as porosity. Atomic force microscopy (AFM) creates detailed topographical and potential maps, crucial for understanding surface roughness and its influence on corrosion behaviour [4,16,21,23]. In the literature, several studies have compared the properties of metallurgically and additively manufactured Ti–6Al–4 V alloys [10,21,24,36–48]. It was established that the microstructure was different (equiaxed grain for metallurgical alloy and lamellar for AM alloy) and that the AM samples usually exhibit reduced corrosion resistance in chloride-containing solution, ascribed to the difference in microstructure and the presence of pores and defects [36–38,41–43]. Most studies dealt with Ti–6Al–4 V prepared by the PBF process, SLM or EBM [10,36–38,40,41–44,46,47,48]. In fewer studies, DED-LB processes were exploited [15,17,27,28,45,49,50]. Furthermore, the corrosion resistance of alloys manufactured by DED-LB has been addressed less extensively [49]. Therefore, there is a lack of comparison between conventional, metallurgically manufactured, and DED-LB-manufactured titanium alloys.

Corrosion resistance is vital for the biocompatibility of titanium alloys in medical applications [51–53], where the material is exposed to various body fluids [2,16,23]. It was studied using electrochemical measurements in simulated physiological environments, including NaCl solution [54], Hanks' balanced salt solution (HBSS) [7], and artificial saliva (AS) [8]. NaCl solution, mimicking saline conditions within the body, is crucial for evaluating resistance to chloride-induced pitting. HBSS simulates human blood plasma's ionic composition, assessing general corrosion resistance, whereas AS reflects corrosion behaviour in the oral environment, which is relevant for dental applications.

This study compares the microstructural and corrosion properties of wrought metallurgically and DED-LB-manufactured Ti–6Al–4 V alloys. Surface analysis was conducted using XRD, 3D profilometry and X-ray photoelectron spectroscopy (XPS) coupled with advanced SEM/EDS/AFM microscopy and scanning Kelvin probe force microscopy (SKPFM). This study continues our recent study [55], which can be taken as a benchmark for the metallographic preparation and characterisation of the wrought Ti–6Al–4 V alloy and further comparison with the DED-LB fabricated alloy.

2. Experimental

2.1. DED-LB setup and samples

Using the DED-LB experimental setup schematically shown in Fig. 1a, the Ti–6Al–4 V (Grade 23) samples in the shape of thin walls were fabricated from the TEKMAT™ Ti64–105/45, plasma atomised powder, Sherbrooke, Canada, with particle size between 30 and 160 μm). In the setup, an annular laser beam DED head with axial powder delivery was used [56]. A fibre laser with a wavelength of 1080 nm and a maximum laser beam power of 2.5 kW was applied as the energy source. The DED-LB process was performed in a build chamber with a controlled argon (inert) atmosphere to avoid powder and deposited layer oxidation. During the process, the presence of oxygen was monitored using a sensor with a resolution of 0.1 % to keep more than 99.6 % inert atmosphere. An IR camera (Optris PI 640), which records the thermal radiation emitted by the side of the wall with a frequency of 10 Hz, was used to characterise the DED-LB fabrication of a thin wall.

With the presented DED-LB setup, thin-wall samples with dimensions of length × height × width = 70 mm × 3 mm × 20 mm were fabricated with a unidirectional deposition of 20 layers. The powder mass flow rate was 6 g/min, and the substrate feeding rate was 5 mm/s. The fabrication of the thin wall started with an initial laser beam power of 1150 W, which was reduced by 10 W per deposited layer. A dwell time of 5 s was used between the successive layers. The 3 mm-thick walls produced with DED-LB were machined from both sides by milling to a uniform thickness of 2 mm. Three disc samples with a diameter of 15 mm were then cut from the milled wall (left, centre and right), Fig. 1b. The characterisation and analysis were performed on the sample from the centre of the manufactured wall unless otherwise stated.

For the comparison, the metallurgically produced wrought titanium alloy Ti–6Al–4 V (Grade 5), a 2 mm thick sheet, was supplied from GoodFellow, Cambridge, England. The sheets were cut into discs with a diameter of 15 mm.

Wrought and DED-LB samples were metallographically prepared in three mechanical and chemo-mechanical steps: (i) water-grinding using MD Mezzo 220, (ii) polishing using MD Largo+DiaPro, 9 μm and (iii) chemo-mechanical polishing using MD Chem+OP-S (SiO_2, 0.25 μm + 10 % v/v H_2O_2) [55]. All polishing cloths and lubricants were distributed by Struers (Ballerup, Denmark).

2.2. Microstructure and surface characterisation

The alloys' microstructure was examined using an optical microscope (ZEISS Axio Imager Z1) at magnifications between 100 × and 1000 × . Before optical microscopy, the sample's surface was chemo-

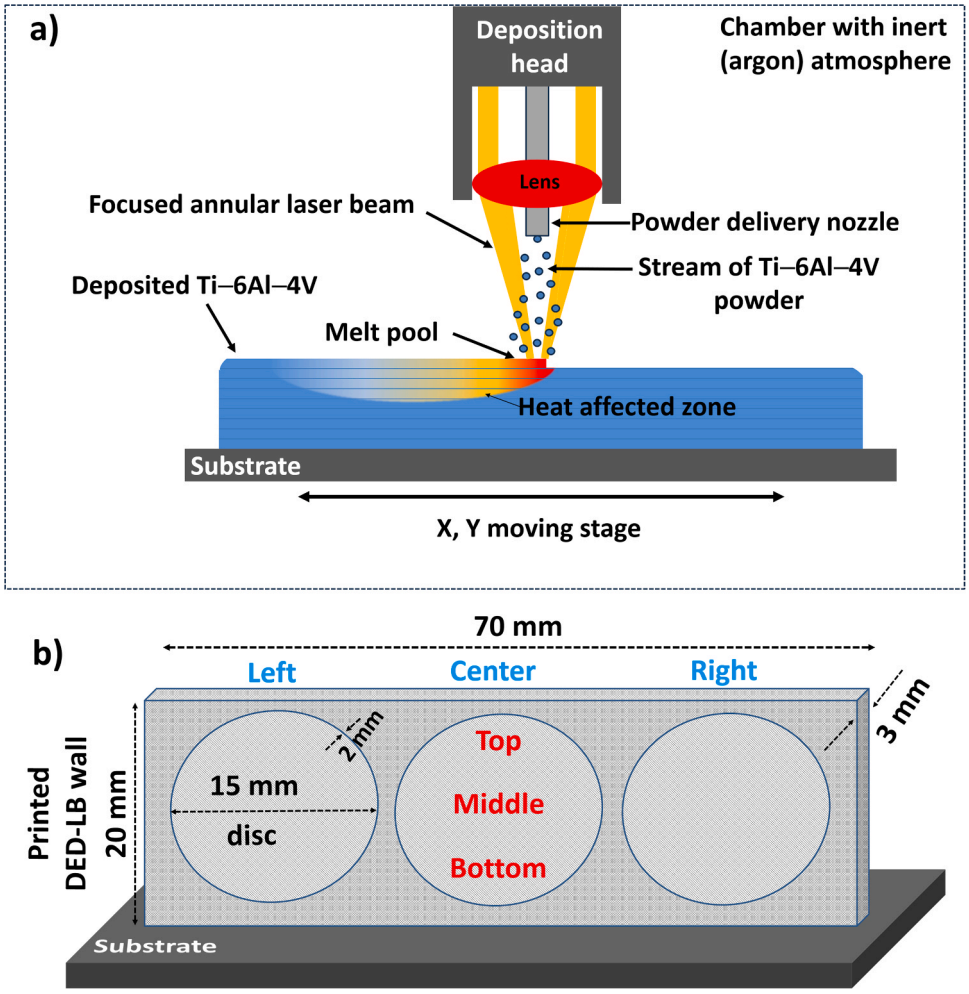

Fig. 1. a) The scheme of the DED-LB system and process, and b) the scheme of the printed wall after machining from which the disc samples were cut.

mechanically polished as described above and then etched for 40 s using Kroll's solution comprising 100 mL water, 4 mL nitric acid (HNO_3), and 2 mL hydrofluoric acid (HF).

The XRD characterisation was performed on a 1 cm^2 sample area on an X-ray powder diffractometer (PANalytical X'Pert PRO) with Cu Kα radiation in the range from 30 ° to 90 ° 2Θ with a step of 0.0033° 2Θ and 100 s per step. The qualitative and quantitative analyses were done by the X'Pert HighScore 4.9 program (Malvern Analytical B.V., Almelo, The Netherlands).

SEM analysis was conducted using a FEI Helios 650 Nanolab instrument (Thermo Fisher Scientific), operating at a beam acceleration voltage of 10 kV. Imaging was performed with a circular back-scattered (CBS) detector for back-scattered electrons (BSE) to obtain compositional information, as they provided a contrast between areas with different chemical compositions. Some images were recorded using a high-performance ion conversion and electron (ICE) detector for secondary ions (SI) and electrons (SE). In addition to SEM analysis, EDS was conducted using an Oxford Instruments AZtec system with an X-max SDD (50 mm^2) detector at 10 kV. The SEM characterisation was conducted in 90 μm × 16 μm area (5000 × magnification) or 3 μm × 2 μm area (20,000 × magnification).

SKPFM and AFM topography measurements were conducted using an AFM LiteScope (NenoVision) integrated within a Versa SEM (FEI, Hillsboro, Oregon, USA). During SEM imaging, the BSE signal was simultaneously captured using a CBS detector to enhance material contrast.

XPS analysis was conducted using a TFA Physical Electronics Inc. spectrometer featuring a hemispherical analyser. The analysis was carried out under a vacuum of approximately 10^{-9} bar. All spectra were recorded using a monochromatic Al Kα X-ray source (1486.6 eV) with a 400 μm diameter analysis area. Survey scans were performed at a pass energy of 187.9 eV, while core-level peaks were measured at 29.4 eV with a 0.1 eV energy step. The emission angle relative to the sample surface was 45°. Binding energies (E_b) were calibrated by referencing the C 1 s peak at 284.8 eV. Chemical composition was quantified using MultiPak software (Version 8.1).

Depth profiles of the oxide layers were obtained at a sputtering rate of 1.0 nm/min, calculated using an Al_2O_3 layer of known thickness deposited by atomic layer deposition. The oxide layer thickness was determined from the depth profile by two methods: the thickness related to the time at the intersection of the Ti 2p and O 1 s curves and the thickness related to the time at the intersection of the Ti 2p metal and Ti 2p oxide curves. The Linear Least Squares (LLS) fitting tool in MultiPak determined the latter. This tool decomposes the Ti 2p spectra into Ti-oxide and Ti-metal components, and the oxide layer thickness is determined at the intersection.

2.3. Electrochemical characterisation

Electrochemical measurements were conducted using a custom-built polymethylmethacrylate three-electrode cell with a volume of 250 mL and a thermostatic jacket to maintain the cell temperature at 37 ± 0.1 °C during the measurements. The sample (wrought and DED-LB fabricated), with an exposed surface area of 1 cm^2, was the working

electrode placed in the cell at the bottom using a holder. A saturated silver/silver chloride (Ag/AgCl) electrode with a potential of 0.197 V vs. the standard hydrogen electrode was used as the reference electrode, while a 5 mm diameter graphite rod functioned as the counter electrode. All electrochemical tests were performed using a multipotentiostat/galvanostat Autolab PGSTAT M204 (Metrohm Autolab, Nova software 2.1.6, Utrecht, The Netherlands).

The sample was first stabilised at open-circuit potential (OCP) for 1.5 h. The electrochemical impedance spectroscopy (EIS) was then conducted in the frequency range from 100 kHz to 10 mHz with a 10 mV amplitude (rms) signal. After completion of the EIS step, the potentiodynamic polarisation curve (PDP) was recorded at a scan rate of 1 mV s^{-1} , starting from −0.15 V vs. OCP and progressing up to 6.0 V. Electrochemical parameters, including corrosion potential (E_{corr}) and corrosion current density (j_{corr}), were extracted from the PDP curves using Nova 2.1.6 software. Representative measurements were chosen to plot them in the graph, and mean values of electrochemical parameters with standard deviations were provided in tables.

Electrochemical measurements were conducted in three simulated physiological environments (Table 1): (1) 0.9 wt% NaCl solution (neutral pH), (2) Hanks' balanced salt solution (HBSS) [7], and (3) artificial saliva (AS) [8]. All chemicals were analytically pure and distributed by Sigma Aldrich.

3. Results and discussion

3.1. DED-LB fabrication of Ti–6Al–4 V samples

Fig. 2 illustrates the steps from raw powder material (Ti-6Al-4V TEKMAT™ Ti64–105/45) to the thin wall samples produced by the DED-LB process (Fig. 2a). The composition of powder particles of Ti 89.0 wt%, Al 6.5 wt% and V 4.5 wt% was determined by EDS (inset in Fig. 2a). The powder of spherical morphology exhibits a Gaussian-like particle equivalent diameter distribution in the range between 30 μm and 160 μm with a mean and standard deviation of 88.6 μm and 21.3 μm, respectively (Fig. 2b). The particle shape and size distribution ensure consistent flowability needed for successful powder feeding and deposition.

Fig. 2c and d show the top and side views of a Ti–6Al–4 V thin wall of dimensions 70 mm × 20 mm × 3 mm deposited on a Ti–6Al–4V substrate of dimensions 90 mm × 15 mm × 3 mm. The images highlight the well-defined rectangular shape of the wall (Fig. 2d) with uniform wall thickness (Fig. 2c), which indicates a high process stability. After DED-LB fabrication and post-processing by milling, three discs were cut from the fabricated wall at three positions (left, centre and right regions) as indicated in Fig. 2d for further microstructure, compositional and electrochemical analyses.

Fig. 3 illustrates an example of the radiation temperature field of a Ti–6Al–4 V wall captured during the DED-LB deposition process by the IR camera. The colour scale on the right represents radiation temperature, which differs significantly from the absolute temperature mainly due to emissivity dependence on the temperature, surface orientation and surface properties. Nevertheless, the laser beam deposition point, located at the top centre of the image, represents the hottest zone of the melt pool with temperatures above the melting point of 1604 °C of the Ti–6Al–4 V alloy. Therefore, the radiation temperature field provides qualitative information on the absolute temperature field. From there, the temperature gradient can be observed by following the colour change from orange through shades of violet and blue to the coldest area in dark blue. By deposition along the layer and by deposition of further layers, each location in the wall experiences fast cyclical cooling and reheating with characteristic directions of the temperature gradient and the resulting heat flow.

Table 1
The composition of simulated physiological solutions used in the study.

Simulated physiological solution	Composition
Hanks' balanced salt solution (HBSS)	8 g/L sodium chloride (NaCl), 0.4 g/L potassium chloride (KCl), 0.19 g/L calcium dichloride dihydrate ($CaCl_2 \times 2\ H_2O$), 0.06 g/L magnesium sulfate ($MgSO_4 \times 7\ H_2O$), 0.40 g/L magnesium chloride hexahydrate ($MgCl_2 \times 6\ H_2O$), 0.35 g/L sodium hydrogen carbonate ($NaHCO_3$), 1 g/L glucose (D-Glucose), 0.25 g/L potassium dihydrogen phosphate ($NaH_2PO_4 \times H_2O$), 0.06 g/L disodium hydrogen phosphate ($Na_2HPO_4 \times 2\ H_2O$); pH ~ 7.2–7.4.
0.9 wt% NaCl solution	9 g/kg NaCl (pH ~ 5.8)
artificial saliva (AS)	0.40 g/L NaCl, 0.40 g/L KCl, 0.69 g/L $NaH_2PO_4 \times 2\ H_2O$, 0.795 g/L $CaCl_2 \times 2\ H_2O$, 0.005 g/L sodium sulphide nonahydrate ($Na_2S \times 9\ H_2O$) and 1.00 g/L urea ($CO(NH_2)_2$); pH ~ 6.8.

3.2. Microstructural and surface characterisation of DED-LB and wrought Ti–6Al–4V samples

3.2.1. Mictrostructural analysis by optical microscopy

To compare the wrought and DED-LB Ti–6Al–4 V, first, a visual overview of the surface appearance is presented in Fig. S1. Metallographic surface preparation through mechanical grinding and chemo-mechanical polishing is highly effective on Ti–6Al–4 V due to the inherent mechanical properties of this alloy. Ti–6Al–4 V exhibits a high degree of toughness and wear resistance, but during polishing, the material's ductility allows for the deformation of surface asperities, as described in our previous study, resulting in a uniform surface finish (Fig. S1a) [55]. Subsequent chemo-mechanical polishing with an alkaline reagent (silica and H_2O_2) enhances the surface finish by dissolving microscopic irregularities and producing a smooth, mirror-like appearance that mechanical polishing cannot fully achieve [55]. The mirror-like appearance is achieved for both wrought and DED-LB samples (Fig. S1b). However, during grinding and polishing, some occasional defects inherent to additively manufactured alloys were noticed [57], such as lack of fusion and gas pores (Fig. S2).

Since polished samples cannot reveal microstructural differences (Fig. S1), a more substantial comparison was performed after etching with Kroll's reagent [58] (a mixture of nitric acid, hydrofluoric acid, and water). The nitric acid in the reagent oxidises the alloy surface. In contrast, the hydrofluoric acid selectively removes the oxidised layers. Conventionally manufactured Ti–6Al–4 V reveals the more refined, uniform, equiaxed grain structure typical of well-controlled thermal and mechanical processing (Fig. S1c).

In contrast, the DED-LB sample shows a lamellar structure, which differs significantly from the wrought sample (Fig. S1d). This difference is primarily related to the localised, layer-by-layer deposition process (Fig. 1), which induces directional solidification and produces an irregular grain structure (Fig. S3).

Images recorded at higher magnification (Fig. 4) clearly show the differences between the etched samples. Since wrought Ti–6Al–4 V alloys are usually produced below β transus temperature of 981 °C [59], such thermal treatment produces a recrystallised microstructure having fine equiaxed α grains, with a dispersion of β at primary α grain boundaries (Fig. 4a,b) [46,60]. Equiaxed microstructures are characterised by small (3 −10 μm), rounded grains with aspect ratios near unity (inset in Fig. 4b) [24].

Etched DED-LB samples show a typical martensite structure with prior β grains (Fig. 4c, d). DED-LB comprises a complex thermal history, including many layers built one above another, each going through a complex history of melting and cooling (Fig. 3), resulting in a columnar structure. Namely, metal powder is first heated above the β transus temperature during DED-LB and cooled down relatively fast (cca. 100 °C/s for DED) [57]. At such cooling rates from the β phase into the α+β field, typically lamellar microstructure is formed, referred to as Widmanstäten α (or α' or acicular α phase), i.e. β → α′ (martensite hcp

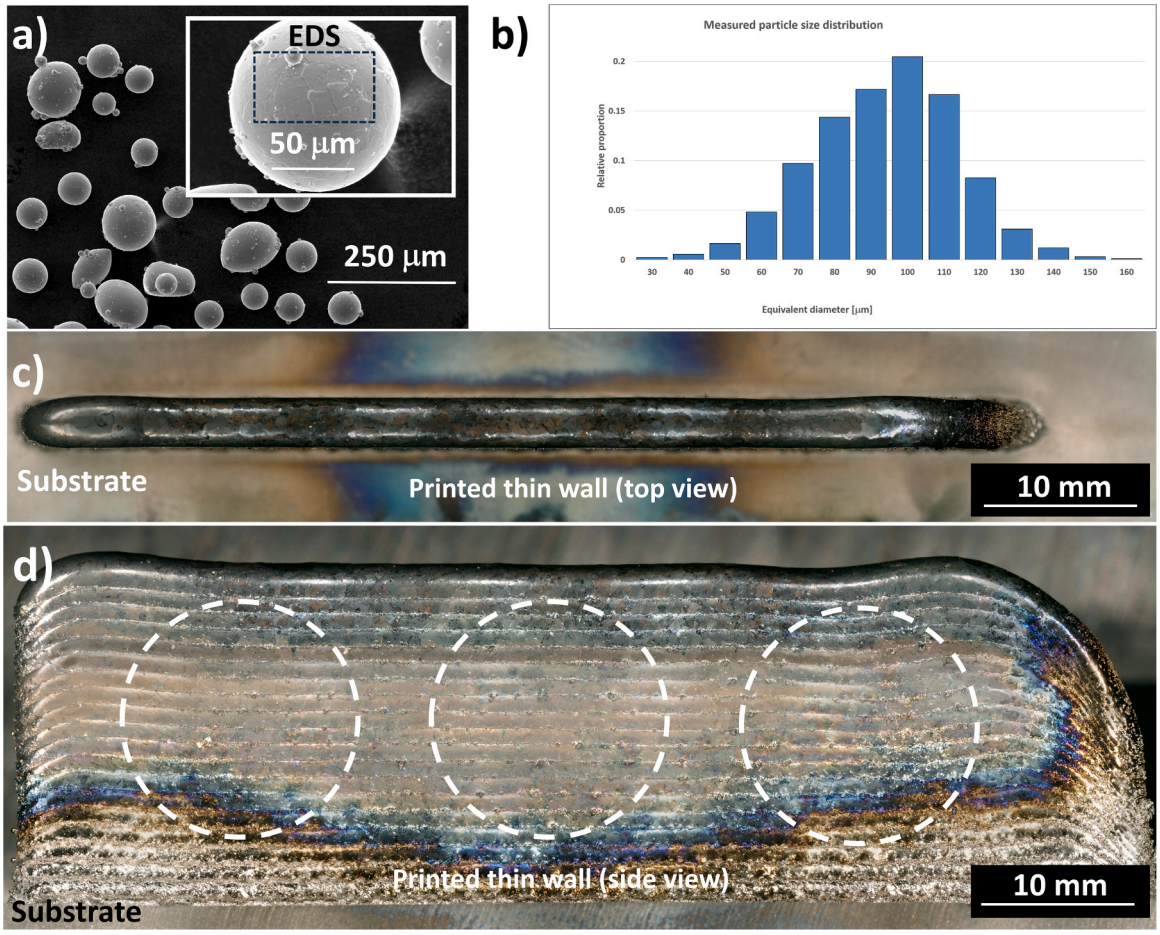

Fig. 2. a) The size and shape of the TEKMAT™ Ti–6Al–4 V powder used in the DED-LB system b) particle size distribution, c) top view, and d) side view of the DED-LB Ti–6Al–4 V thin wall deposited on the substrate. The notation of the samples depending on the position is described in Fig. 1.

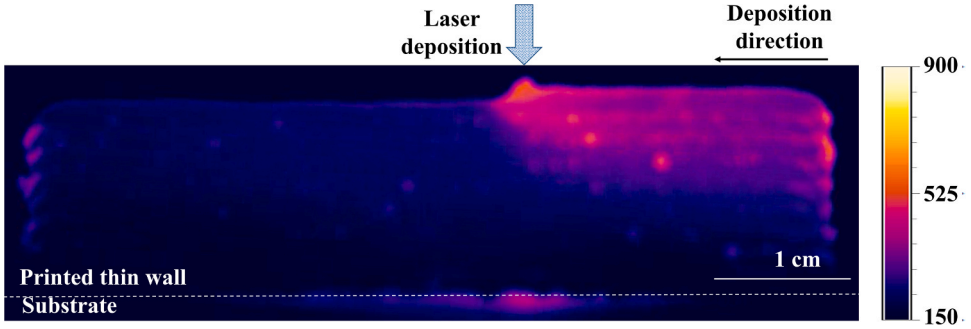

Fig. 3. The radiation temperature field captured by an IR camera during the fabrication of a thin wall by the DED-LB deposition of Ti–6Al–4 V powder.

phase) transformation. The martensitic transformation starts at cca. 650 °C [60]. There are two main types of martensite: one with a twinned structure, known as acicular (needle-shaped) martensite, and the other with a high density of dislocations but few or no twins (massive martensite) [61]. In the current study, the former is observed and denoted as α'. These coarse α' grains (α' plates or needles) have a specific martensite crystallographic orientation within grains of the β matrix [60]. Acicular α' phase nucleates from grain boundary α, forming α colonies whose size and shape are dictated by prior β grain boundaries and within prior β grains [62,63] denoted in Fig. 4c,d. SEM images of etched wrought and DED-LB samples are presented in Fig. S4. Martensite acicular structure was observed for SLM-manufactured Ti–6Al–4 V alloys [21,41,43,44,48,64].

In summary, conventionally manufactured Ti–6Al–4 V samples have a fine, more uniform α+ β structure. DED-LB Ti–6Al–4 V exhibits a more heterogeneous and directional grain structure, with more prominent α' acicular grains formed within the grains of the β-phase matrix. The repetitive thermal cycle in the heat-affected zone (reheating and recooling) impacts the material's microstructure, promoting the formation of distinct Widmanstäten α' acicular phase aligned with the direction of heat flow. The control of this thermal gradient is crucial for maintaining material consistency [32], minimising defects, and achieving optimal crystallisation of the material (without any residual powder in the structure) [65] and desired properties in the manufactured DED-LB alloy [34]. The effect of these microstructural differences on compositional, morphological and protective properties is further addressed in the

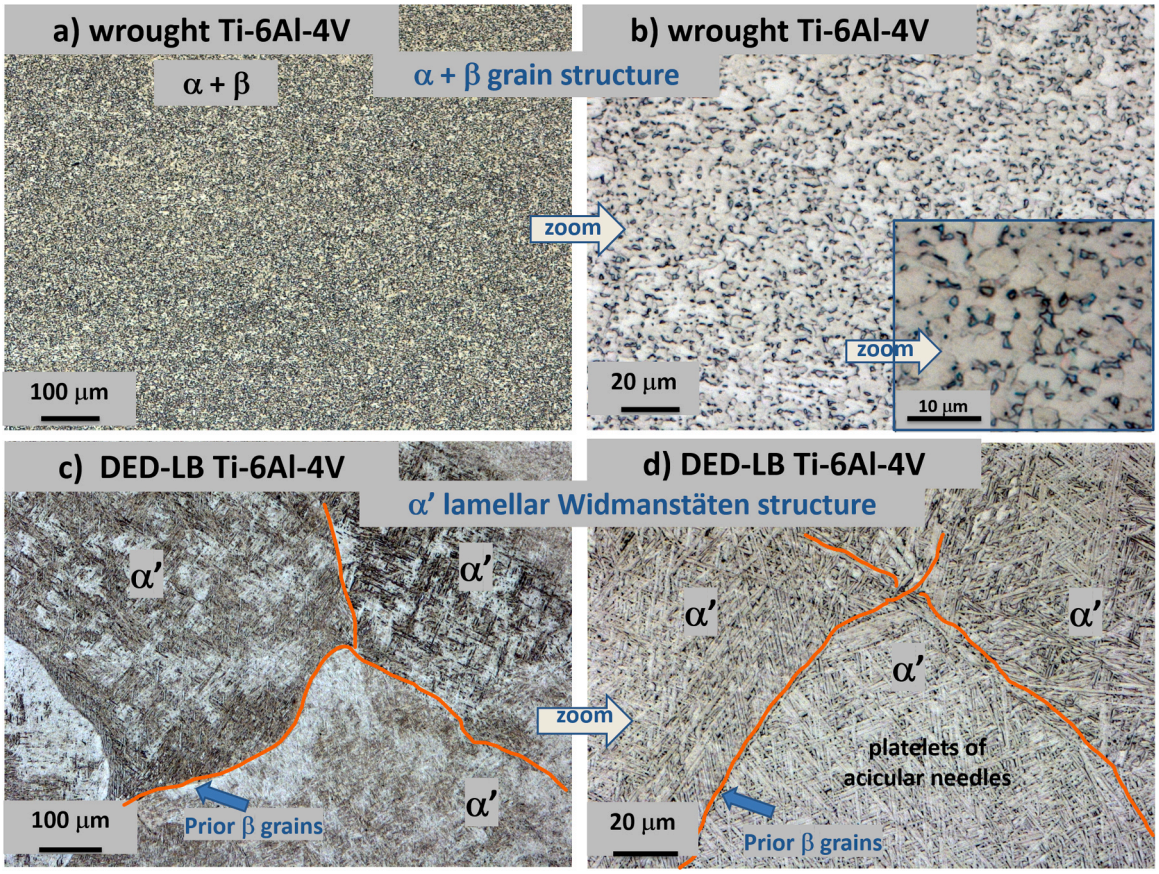

Fig. 4. Microstructural differences under the optical microscope of the conventionally manufactured wrought and DED-LB additively manufactured Ti–6Al–4 V alloys. Samples were (a, b) chemo-mechanically polished and (c, d) additionally etched with Kroll's reagent. Grain boundaries of prior β grains are highlighted by orange lines.

following sections.

3.2.2. *Phase composition by XRD analysis*

The X-ray diffraction patterns of the wrought and DED-LB Ti–6Al–4 V samples are shown in Fig. 5. The wrought alloy exhibits well-defined peaks, reflecting the stable two-phase (α+β) microstructure, where Al stabilises the α-Ti phase and V stabilises the β-Ti phase. The conventional manufacturing process involves thermal treatments such as forging or annealing, which allow sufficient time for the diffusion-controlled transformation of the β-phase to the equilibrium α-phase [62]. The prominent XRD peaks are aligned with α-Ti (hcp) phase (ICDD PDF#04–023–7232) with the main peaks at 35.3°, 38.5°, 40.4°, 53.2°, 63.4° and 76.7° (2θ) (crystallographic orientations are denoted in the figure). Additionally, peaks related to the β-Ti (bcc) phase (ICDD PDF#04–018–5433) were noted at 39.6°, 57.2° and 71.8° (2θ). Based on analysis of the XRD spectrum, the wrought sample contains 98.6 % of the α (hcp) phase and 1.4 % of the β (bcc) phase.

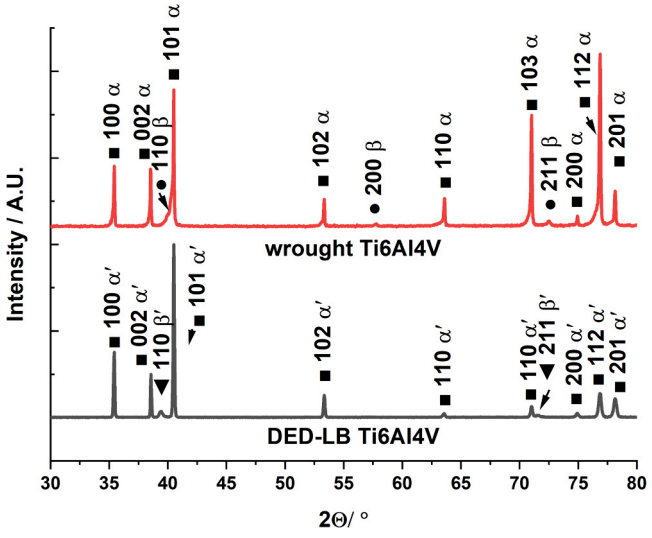

Fig. 5. The XRD diffraction (normalised) patterns of the wrought and DED-LB Ti–6Al–4 V alloys. Both alloys contain predominantly α/α'-Ti and some peaks related to the β-Ti phase.

The XRD diffraction pattern for the DED-LB sample also confirmed the predominance of α-Ti (Fig. 5). α-Ti (hcp) and α'-Ti (hcp) phases cannot be differentiated by XRD; the spectrum of DED-LB samples is thus regarded as martensite α'-Ti phase since the latter has been proven by optical microscopy in Fig. 4. In addition, peaks related to the β-Ti phase were noted, but at slightly lower position than those observed for the wrought sample. The position of the peaks is aligned with the β phase (ICDD PDF#01–081–9813) with the prominent peaks at 39.4°, 56.9° and 71.4° (2θ). These peaks are denoted as β'-Ti since they are positioned slightly differently from the β-Ti of the wrought alloy. It is difficult to state with assurance that these are two different β-Ti phases or the same phases but that the peaks are shifted due to the different thermal histories of the two processes. Calculations based on the XRD spectrum show that in the DED-LB sample, the α (hcp) phase represents 99.5 % and the β (bcc) phase 0.5 %, indicating a lower amount of β phase, aligned with the relatively fast cooling from the high temperature and insufficient time for the recrystallisation of the β phase.

Similar XRD patterns were observed in the literature for AM Ti–6Al–4V, mainly regarding SLM-deposited samples. In some studies,

exclusively α (or α')-Ti (hcp) phase were noted [41,44,48,66,67], whereas in other studies, peaks related to β-Ti (bcc) phase were also noted for SLM samples [10,42,43,59], EBM samples [68] and DED samples [49]. The presence of α"-Ti (orthorhombic) phase was also noted for the SLM samples [64].

According to literature data [10], AM Ti–6Al–4 V samples showed higher residual stresses related to a high density of dislocations and lattice distortion [10]; residual stresses are typically minimised through post-processing treatments, such as annealing [21,46,47,49]. In the present work, the amount of residual stress was not quantified, but it can be hypothesised that DED-LB also results in a certain amount of residual stress, as shown by other AM-manufactured samples [49]. This issue will be addressed in our forthcoming study.

The XRD diffraction analysis of Ti–6Al–4 V alloys produced by conventional and additive manufacturing reveals minor differences in microstructural characteristics. While the wrought sample shows a stable, well-characterised two-phase microstructure with a balanced distribution of α and β phases, the DED-LB process generates a more refined microstructure with α'-martensite.

3.2.3. *Morphology and chemical composition by SEM/EDS analysis*

First, the difference in microstructure between the DED-LB and wrought samples was investigated (Fig. 6). Second, for the DED-LB sample, the effect of the position and height in the printed wall on the microstructure was addressed (Fig. 7).

The BSE images differ in the composition related to the atomic number; the higher the atomic number, the brighter the material appears in the image. The microstructure of the wrought sample predominantly consists of a α phase matrix interspersed with intergranular β phase [6,11,55] (Fig. 6a). In the BSE image, the α matrix appears as darker regions due to the predominantly Ti content containing around 6 wt% of lighter Al [55] (inset in Fig. 6a). The V-rich phase appears as brighter regions due to the higher atomic number of V compared to Ti [55]. EDS compositional analysis was made at different locations of the area imaged. First, the whole area imaged in Fig. 6a was analysed, giving 89.6 wt% Ti, 6.2 wt% Al and 4.2 wt% V (results written within the image). Local chemical composition made at different locations, numbered from 1 to 5 (Table 2), differs from that determined at the larger scale. Sites 1 and 2 refer to α matrix grains containing only Ti and Al (about 94 wt% Ti and 6 wt% Al). Sites 3 and 4 refer to β-phase grains containing less Ti and less Al than α grains, but are abundant in V (about 16 wt%). Some grains (site 5) contain a high amount of Ti and Al as α grains and a small amount of V (about 3 wt%).

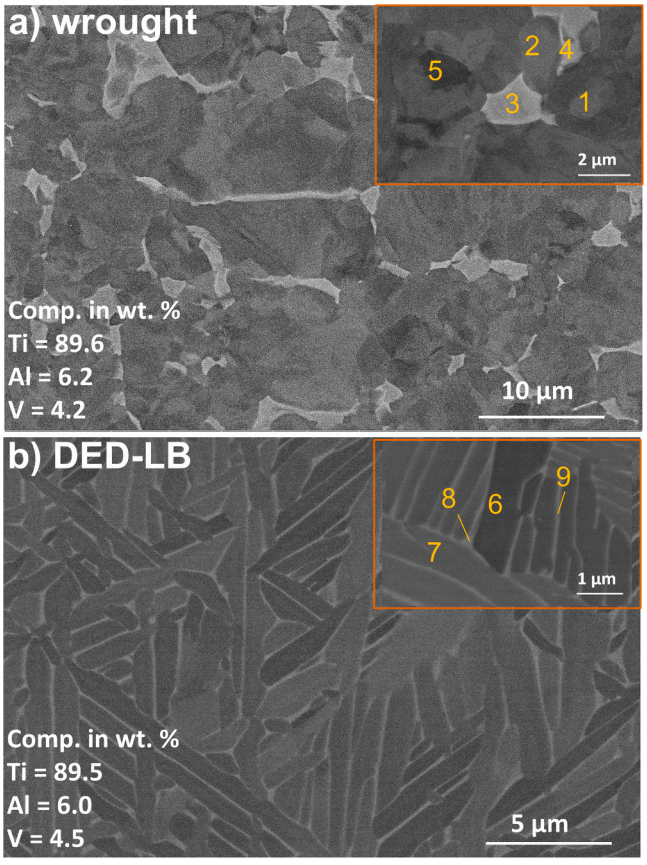

Fig. 6. Back-scattered SEM images of surface morphology of chemo-mechanically polished a) wrought and b) DED-LB manufactured Ti–6Al–4 V samples at low (5000 ×) and high (20,000 ×) magnification (insets). The sample was cut from the bottom middle position of the printed wall (Fig. 1). The composition of the samples determined by EDS analysis on the area imaged by SEM is given in the images. EDS results for numbered sites are shown in Table 2.

In contrast, the microstructure of the DED-LB Ti–6Al–4 V sample (Fig. 6b) exhibits a distinct bimodal character, significantly different from the equiaxed grain structure commonly observed in wrought Ti–6Al–4 V alloys (Fig. 6a). The refined lamellar structure in the DED-LB alloy can enhance mechanical performance by providing barriers to dislocation movement, which is critical for improving the material's strength and resistance to fatigue [11,24]. EDS compositional analysis of the area imaged in Fig. 6b was 89.5 wt% Ti, 6.0 wt% Al and 4.5 wt% V (results written within the image), i.e., comparative to the wrought alloy. Local chemical compositions are represented by sites from 6 to 9 (inset in Fig. 6b). Sites 6 and 7 refer to lamellar Al-rich α phase containing about 90 wt% Ti, 6 wt% Al, and 2 −3 wt% V. This phase is typically aligned with the solidification direction, a feature driven by the directional cooling inherent to the DED-LB process. The lamellae are embroidered with the V-rich phase (sites 8 and 9). These sites contain less Ti and Al, and more V (8 −9 wt%) than the α phase.

EDS confirmed the presence of the key alloying elements Ti, Al, and V in both samples in very similar concentrations (Fig. 6). Thus, despite the differences in microstructural features, the DED-LB process effectively maintains the chemical integrity of the alloy, ensuring that the alloy's composition remains within the specifications required for its intended applications [25]. However, microstructural differences induce differences in chemical composition at the local micrometre level. A clear distinction between the wrought and DED-LB samples is the distribution of vanadium. In the wrought sample, V is concentrated predominantly in β-phase grains, reaching about 16 wt%. These V-rich grains are surrounded by an α-matrix. In the DED-LB sample, V is concentrated in the longitudinal β-phase at a smaller content (8 −9 wt %) than in the wrought sample, but it is also present in the matrix phase (2 −3 wt%). Thus, the V concentration is smaller in individual locations in printed than in wrought alloy, but it is spread over the entire matrix surface.

Next, the BSE SEM images of DED-LB Ti–6Al–4 V samples were recorded at a high magnification of 20,000 × for samples extracted from three positions within the printed wall (Fig. 1): left, centre, and right (Fig. 7). A consistent microstructure across all positions was observed, with no significant variation in the size, distribution, or morphology of the α and β phases from left to right. This suggests that the wall's edge positions (corners), where thermal gradients might have been expected to influence phase transformation, do not lead to microstructural differences.

Each sample is further examined at three different heights within the wall structure: top, middle, and bottom (Fig. 7). No notable variations in the phase structure, grain morphology or composition determined by EDS were observed. Therefore, the reduction in power during printing (−10 W/layer), designed to mitigate heat input, does not appear to impact the overall microstructure.

In summary, SEM/EDS results demonstrate that the selected printing parameters efficiently produce a well-defined and uniform

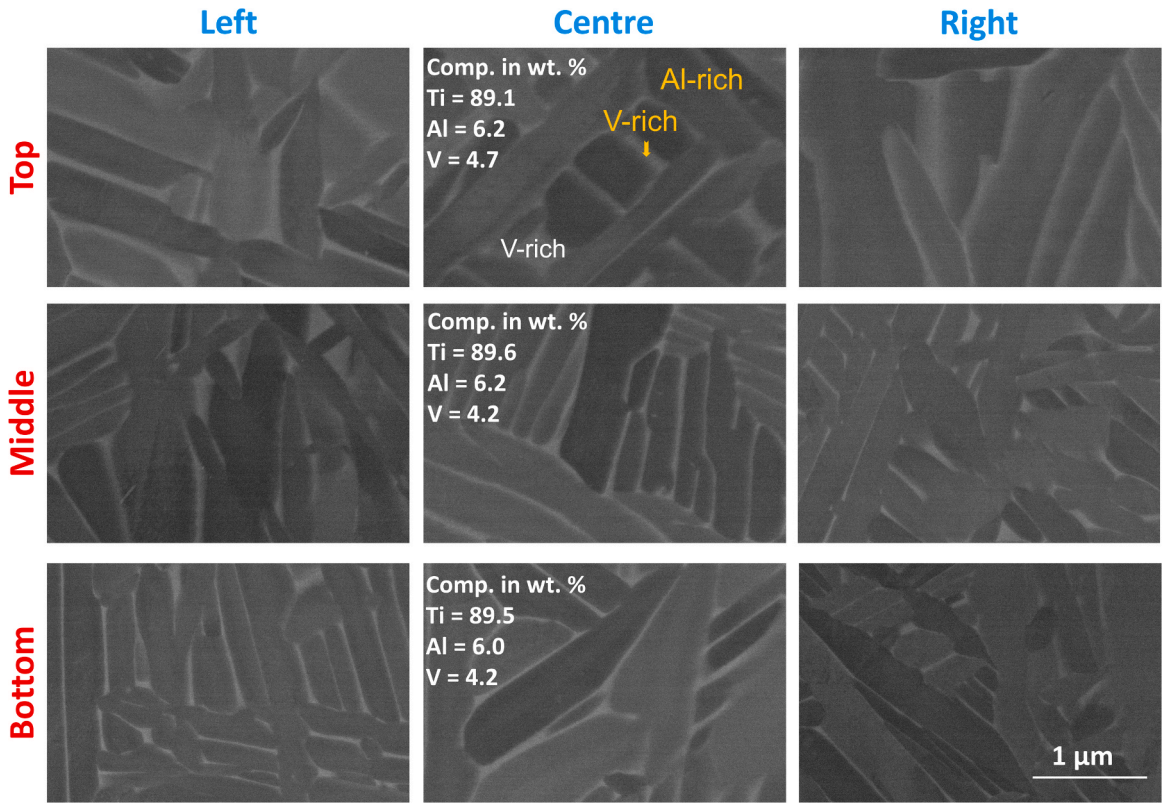

Fig. 7. Back-scattered SEM images of surface morphology of chemo-mechanically polished DED-LB manufactured Ti–6Al–4 V samples at high magnification (20,000 ×) at different horizontal (left, centre, and right) and vertical (top, centre, and bottom) positions in the printed wall (Fig. 1). The values represent the elemental composition given in weight percentages determined by EDS on the area imaged by SEM.

Table 2
Elemental composition in wt% determined by point EDS analysis at numbered sites in Fig. 6 for wrought (sites 1 –5) and DED-LB (sites 6 –9) Ti–6Al–4 V samples.

Site	elemental composition (wt%)		
	Ti	Al	V
	wrought Ti–6Al–4 V		
1	93.4	6.6	-
2	94.2	5.8	-
3	80.8	3.3	15.9
4	79.8	3.5	16.7
5	89.3	6.8	2.8
	DED-LB Ti–6Al–4 V		
6	91.5	6.3	2.2
7	90.5	6.3	3.2
8	85.5	4.8	9.6
9	87.2	5.0	7.8

microstructure, irrespective of the position or height within the printed wall. Pores or lack of fusion were only occasionally observed between the deposited layers, even at high magnifications, confirming that the deposition process produces a homogeneous structure across the entire wall.

3.2.4. Morphology and surface potential difference by SEM/AFM/SKPFM analysis

Optical microscopy imaging after etching with Kroll's reagent (Fig. 4) provided the basis for further localised investigations using combined SEM, AFM and KPFM techniques to correlate surface morphology with compositional variations and surface potential difference (Fig. 8).

Fig. 8a presents a BSE SEM image of the wrought Ti–6Al–4 V sample. Similar to Figs. 6 and 7, it reveals differences between the α (Al-rich)- and β (V-rich)-phases. At the same area (20 µm × 20 µm), the AFM topographical 3D mapping was recorded, providing the surface morphology and roughness at the nanoscale. The roughness (S_a) was 0.9 nm for wrought and 1.1 nm for the DED-LB sample. AFM results (Fig. 8c) showed small topographical changes at the phases, sub-grain surface, boundaries and mechanical polishing marks that SEM may not capture in the CBS mode. The measured surface height variations between 0 and 50 nm reflect a smooth surface, resulting from chemo-mechanical polishing.

The combination of SEM/AFM with SKPFM correlates compositional contrast (from SEM) with surface potential difference variations (from KPFM) (Fig. 8e). The surface potential difference ranges between 0 and 84 mV. By overlaying the CBS SEM compositional image with the KPFM surface potential map, it is possible to correlate the microstructure (phases, grain boundaries) with the electronic properties of the surface. The differences in the surface potentials between the phases are minor and may be related to the surface passivation of the Ti alloys. Upon air exposure, a spontaneously formed oxide layer passivates the surface and minimises the potential differences between the phases in the alloy. This is particularly useful for critical electronic surface characteristics, such as corrosion resistance.

Combined SEM/AFM/SKPFM analysis was also performed for DED-LB Ti–6Al–4 V (Fig. 8b). A typical lamellar shape was confirmed by BSE SEM. The topographical AFM image between 0 and 18 nm revealed a smooth surface with minor differences in the topography (Fig. 8d). Again, a correlation exists between nanometer-scale surface features in α and β-phase or along grain boundaries between SEM and AFM. The variation in the surface potential difference ranges between 0 and 70 mV and is similar to that of the wrought sample (Fig. 8 f). This indicates that the potential differences between the phases are again minor and reflect the surface passivation more than the presence of the individual phases,

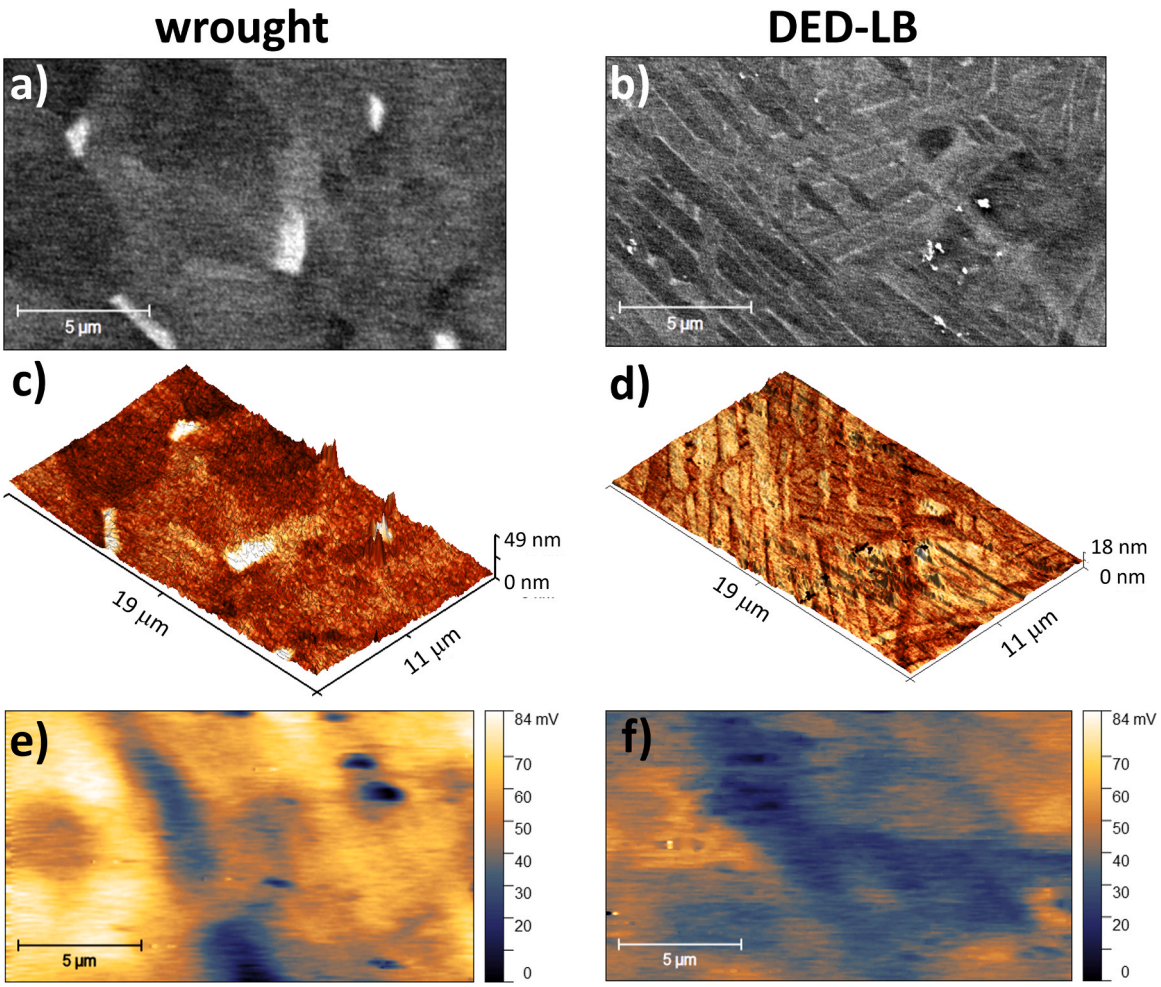

Fig. 8. (a, b) Back-scattered CBS SEM images, (c, d) AFM 3D surface topography, and (e, f) SKPFM surface potential difference analysed at the same area of chemo-mechanically polished (a, c, e) wrought and (b, d, f) DED-LB Ti–6Al–4 V samples.

as observed in ref. [69].

Coupled SEM/AFM/SKPFM provided more detailed information on the Ti–6Al–4 V microstructure. The composition, surface topography, morphology and electronic characteristics (surface passivation) are similar despite the difference in microstructure between wrought and DED-LB alloys. In both samples, the surface characteristics are also strongly related to surface passivation during exposure to the atmosphere.

3.2.5. *Chemical composition by XPS analysis*

XPS analysis was conducted on chemo-mechanically polished DED-LB (the comparative analysis on wrought Ti–6Al–4 V is presented in ref. [55]). The survey spectra of the DED-LB sample confirmed the composition with Ti, O and Al as the primary elements and adventitious carbon (Fig. S5). Vanadium was not detected at the surface, as it is buried below the surface layer, as shown below.

High-energy resolution XPS spectra of Ti 2p, Al 2p, O 1 s, and V 2p were recorded to investigate the chemical states of the elements. Spectra recorded at the surface and a depth of 40 nm are presented in Fig. 9 (spectra at all depths are presented below in Fig. 11). The Ti $2p_{3/2}$ and $2p_{1/2}$ peaks recorded at the surface are located at 458.4 eV and 464.3 eV, respectively, corresponding to the surface passive film of TiO_2 [7,55,70]. In addition to TiO_2, a small Ti $2p_{3/2}$ peak centred around 453.7 eV is noticed, similar to that observed for the wrought sample [55]. This common feature in both types of alloys indicates the presence of regions where the surface oxide layer is either incomplete or very thin, allowing detection of the underlying metal. The reason lies in the chemo-mechanical preparation of the samples, which includes a continuous oxidative action of H_2O_2 and removal by SiO_2 particles, leading to the thinning of the surface layer.

The O 1 s spectrum is centred at 530.4 eV. It comprises components related to O^{2-} species (at 529.9 eV) and OH^- species (at 531.3 eV), consistent with forming a hydrated titanium oxide layer during metallographic preparation (as a result of a chemo-mechanical polishing with alumina nanoparticles and H_2O_2 at pH 8.9). The Al 2p spectrum exhibited a small, unresolved peak at around 74 eV, related to Al_2O_3 [51]. Vanadium was not detected at the surface [7,55]. Therefore, the XPS analysis shows that the surface of the DED-LB sample was mainly composed of a thin TiO_2 layer, similar to that for wrought Ti-6Al-4V alloy under the same surface metallographic preparation [55].

The passivity of wrought Ti-based alloys is primarily based on forming a TiO_2 oxide layer. However, depending on the composition of the alloy, passive film also contains oxides of the alloying elements, i.e. Al_2O_3 for Ti–6Al–4 V [7], Al_2O_3 and Nb_2O_5 for Ti–6Al–7 Nb [71] and Nb_2O_5, Ta_2O_5 and ZrO_2 for Ti–20Nb–10Zr–5Ta [72].

The depth profiles of the DED-LB sample, illustrating the variation in chemical composition with sputtering time, are shown in Fig. 10. The sputtering rate was 1 nm/min. Ti, O, and adventitious C were the dominant elements at the surface. As sputtering progressed, the Ti signal increased while the O signal decreased. The signal for carbon rapidly diminished beneath the surface, while Al and V signals started to emerge as the oxide layer was removed.

The thickness of the oxide layer determined as the intersection of Ti 2p and O 1 s curves is 1.5 nm (Fig. 10a). Using the LLS method, where

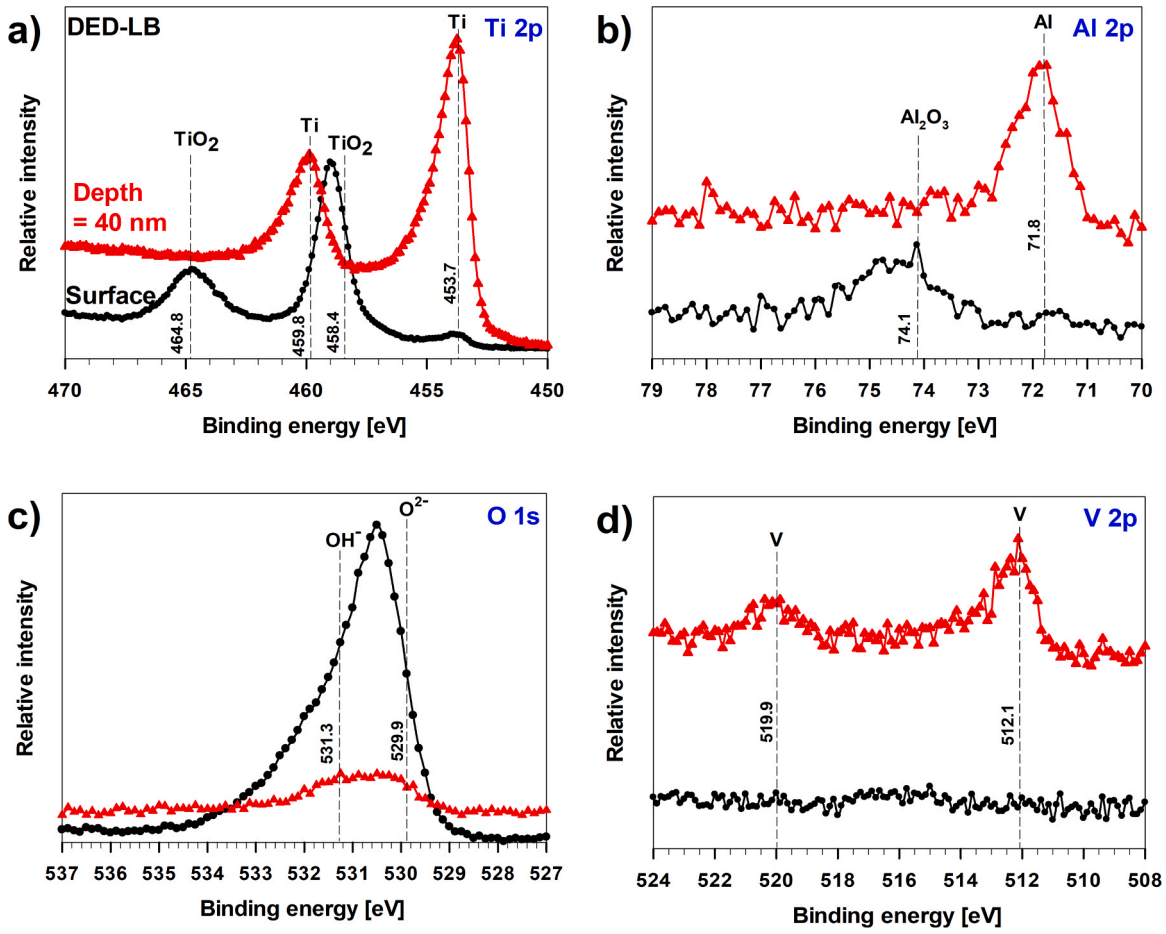

Fig. 9. XPS Ti 2p, Al 2p, O 1 s and V 2p spectra recorded at the surface and a depth of 40 nm of the DED-LB Ti–6Al–4 V sample after chemo-mechanical polishing.

the oxide thickness was determined as an intersection between Ti 2p metal and oxide curves, the obtained value was somewhat smaller, i.e. 1.1 nm (Fig. 10b).

Similar surface compositions were detected for wrought samples [55], but for the DED-LB sample, the spontaneously formed oxide layer was thinner, i.e., 1.1 nm, as opposed to 2.7 nm [55], as determined by the LLS fitting for the wrought sample.

The Ti 2p and Al 2p spectra, tracked over different sputtering times, are presented in Fig. 11. The Ti $2p_{3/2}$ peak shifted from 458.4 eV (associated with TiO_2) to 453.7 eV (indicating metallic Ti) as the sputtering progressed. The Al 2p peak at 74.1 eV related to Al_2O_3 appeared just below the surface, showing that it was buried beneath the outer Ti oxide, consistent with previous findings [51,52,55]. As sputtering reached deeper layers, the Al 2p peak shifted to ~71.8 eV, related to metallic aluminium. By 40 nm, the Ti $2p_{3/2}$ and $2p_{1/2}$ peaks were positioned at 453.7 eV and 459.8 eV, respectively, corresponding to metallic Ti, while the Al 2p peak at 71.8 eV indicated the presence of metallic aluminium and vanadium, respectively.

Vanadium was initially absent in the surface oxide layer but appeared at around 2 nm, increasing its intensity toward the inner interface (Fig. 11) with the $2p_{3/2}$ peak at 512.8 eV of metallic V [7]. The intensity of the O 1 s gradually decreased as the sputtering process proceeded (Fig. 11).

Previous studies on titanium alloys have highlighted that manufacturing can influence microstructure and surface oxidation [10,41]. Although the microstructure of the bulk material may differ due to different cooling rates and thermal histories, the surface chemistry, as detected by XPS, tends to be dominated by the formation of titanium oxides due to the high affinity of titanium for oxygen [14]. In the present study, a very similar surface composition was identified for DED-LB and wrought Ti–6Al–4 V samples [55], predominantly consisting of a hydrated TiO_2 layer with traces of Al_2O_3. The latter was buried just below the surface due to an instantaneous and continuous coverage by TiO_2. Therefore, both processes (conventional metallurgy and DED-LB AM) produce surfaces with similar characteristics in terms of oxide coverage. In both cases, some surface regions of thinner oxide areas are present (indicated by a metallic Ti peak), which could be attributed to surface roughness, processing conditions, or post-processing treatments such as chemo-mechanical treatment. The thickness of the spontaneously formed oxide layer, however, was thinner on the DED-LB sample than on the wrought alloy.

3.3. *Electrochemical measurements and corrosion mechanisms of DED-LB and wrought Ti–6Al–4 V samples*

Electrochemical measurements at OCP and under polarisation assessed the corrosion resistance and characteristics of the passive films formed on wrought and DED-LB Ti–6Al–4 V samples in three physiological solutions: Hanks' balanced salt solution, 0.9 wt% NaCl, and artificial saliva. These measurements provided an understanding of the electrochemical stability of the alloys, revealing differences in their behaviour in different solutions.

3.3.1. *Electrochemical impedance spectroscopy data at OCP*

Electrochemical impedance spectroscopy provided additional insights into the passive oxide film's stability at the OCP. Nyquist plots and Bode plots measured for wrought and DED-LB samples in three investigated solutions, HBSS, NaCl and AS, are presented in Fig. 12. Nyquist

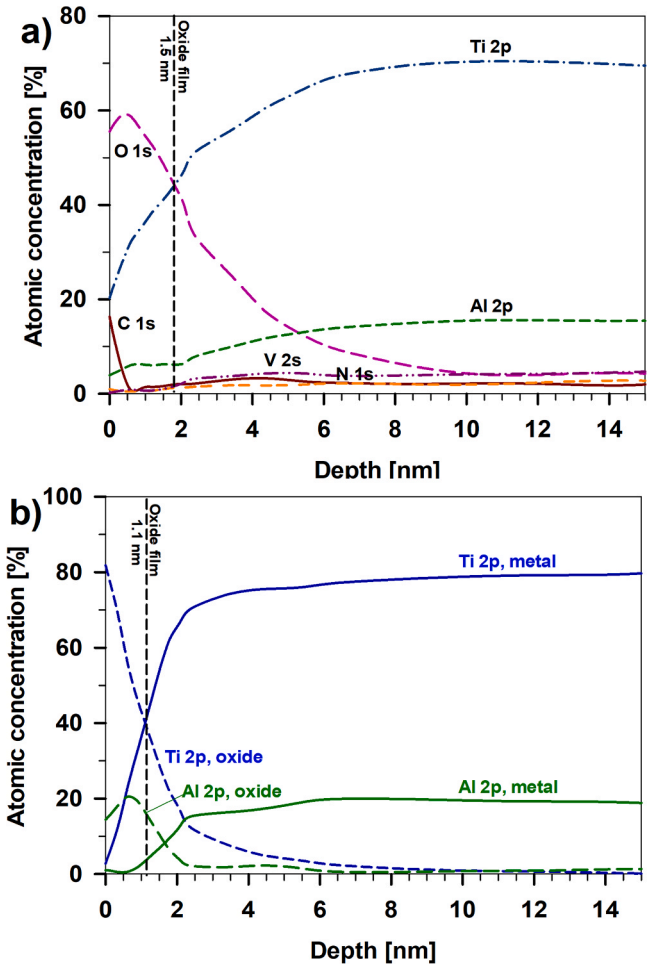

Fig. 10. a) XPS depth profile of Ti 2p, Al 2p, O 1 s, V 2p and C 1 s recorded at the chemo-mechanically polished surface of DED-LB Ti–6Al–4 V sample. The oxide thickness was determined as the intersection between the Ti 2p and O 1 s curves. b) LLS fitting presenting the depth profiles of Ti 2p and Al 2p metal and oxide curves. The oxide thickness was determined as the intersection between the Ti 2p metal and oxide curves. The sputtering rate was 1 nm/min.

plots show semi-circular arcs with the diameter of each arc representing the charge transfer resistance, indicating alloy's corrosion resistance. The diameter of the semi-arcs was smaller for DED-LB samples than for wrought samples, and it decreased from HBSS to AS solutions. Bode plots, featuring the differences in $|Z|$ and phase angle (Θ) vs. frequency (f) across the tested solutions, are characterised by three regions: (i) high f region representing the interface of the surface film with the solution, (ii) middle f region where $|Z|$ is linearly decreasing with f and Θ is constant, and (iii) low f region representing the interface of the surface films and underlying metal, usually related to a decrease in Θ. The trends in the Bode plots showing a broad region of linearity of $|Z|$ vs. f and a broad plateau of Θ vs. f align with the observations from the Nyquist plots, generally confirming the formation of the passive films on both alloys and their protectiveness in simulated physiological solutions.

To quantitatively express the resistance and capacitance properties of the passive films formed on Ti–6Al–4 V samples, equivalent electrical circuit (EEC) models were employed to fit the experimental results (Fig. 13). For HBSS and NaCl solutions, a two-time constant model (Fig. 13b) was used to distinguish the inner and outer oxide layers formed on the surface of the DED-LB sample, while a single-time constant model (Fig. 13a) was sufficient for AS, suggesting the thinner and less stable oxide layer in this solution, consistent with PDP results presented in 3.3.2. EECs contain the components representing solution resistance (R_s), polarisation resistance (R_p) composed of R_1 (inner compact oxide) and outer R_2 (outer porous oxide), and constant phase element (CPE). The latter describes non-ideal capacitive behaviour; CPE_1 (pseudo-capacitance of inner oxide layer) and CPE_2 (pseudo-capacitance of outer oxide layer) were used.

The largest semicircles for the DED-LB alloy were registered in HBSS and corresponded to the highest polarisation resistance ($R_p = R_1 + R_2$) of 3.23 MΩ·cm^2 with a Θ of -71° at 10 mHz (CPE_1 = 20.0 μΩ^{-1}·s^n·cm^{-2}, n_1 = 0.91; CPE_2 = 2.0 μΩ^{-1}·s^n·cm^{-2}, n_2 = 0.88), indicating a compact and stable passive oxide layer (Fig. 12a,c). The wrought alloy in HBSS showed better corrosion resistance, with $R_p = R_1$ = 5.70 MΩ·cm^2, a Θ of -73° at 10 mHz, and a CPE value of 29.2 μΩ^{-1} ·s^n·cm^{-2} (n = 0.93) (Table 3).

In 0.9 wt% NaCl, the intermediate semicircle diameter was registered, showing reduced corrosion resistance of the DED-LB alloy compared to HBSS. R_p decreased to 1.54 MΩ·cm^2, respectively, while the Θ at 10 mHz decreased to -68°. The R_s value increased slightly to 88 Ω·cm^2, and the capacitance values to CPE_1 = 26.5 μΩ^{-1} ·s^n·cm^{-2} and CPE_2 = 5.6 μΩ^{-1} ·s^n·cm^{-2} (n_1 = 0.93 and n_2 = 0.82) indicated a less compact oxide layer in comparison with HBSS. The wrought alloy outperformed the DED-LB alloy in NaCl, achieving a higher R_p of 8.09 MΩ·cm^2 and a Θ at 10 mHz of -81°. The lower value of CPE_1 = 20.50 μΩ^{-1} ·s^n·cm^{-2} (n_1 = 0.94) suggested fewer defects and a more homogenous passive oxide layer formed on wrought alloy.

The diameter of the semicircle of DED-LB Ti–6Al–4 V was further reduced in artificial saliva, suggesting the lowest corrosion resistance compared to HBSS and NaCl. R_p was 0.642 MΩ·cm^2, i.e. fivefold and over twofold smaller than in HBSS and NaCl, respectively; the phase angle at 10 mHz dropped to only -49°, indicating that the passive oxide layer in AS has lower corrosion resistance. Obtained values of CPE_1 = 26 μΩ^{-1} ·s^n·cm^{-2} and n = 0.91 suggest a thinner, more porous and less compact oxide layer, possibly due to differences in the solution chemistry in AS, which may prevent the formation of the well-defined multilayered passive oxide film. In contrast, the wrought alloy demonstrated better R_p = 8.80 MΩ·cm^2, a Θ at 10 mHz of -84°, and CPE of 24.5 μΩ^{-1} ·s^n·cm^{-2}.

The Bode plots further emphasised these differences, particularly in the impedance magnitude and phase angle (Fig. 12b,d). In HBSS, the DED-LB alloy showed the highest $|Z|$ values at low frequencies (10 mHz), confirming the excellent protective properties of its passive oxide layer. The Θ remained close to -80° over a broad frequency range, indicative of a highly capacitive oxide film. In 0.9 wt% NaCl, $|Z|$ values were lower, and the Θ dropped to -68°, showing reduced film compactness. In AS, the lowest $|Z|$ and Θ values (-49° for DED-LB) were achieved, showing the lower stability and protective capacity of the oxide layer.

Table 3 summarises the EIS parameters, including R_p (R_1, R_2), R_s, CPE and Θ at 10 mHz values, for the DED-LB and wrought samples in HBSS, 0.9 wt% NaCl and AS. These quantitative results provide evidence of the corrosion resistance of the passive film of the DED-LB alloy, particularly in HBSS, where its R_p and CPE values indicate a compact and stable passive oxide layer. The wrought alloy generally demonstrated better corrosion characteristics in all solutions, with R_p ranging between 5.7 MΩ·cm^2 and 8.8 MΩ·cm^2 (compared to 0.64 MΩ·cm^2 and 3.23 MΩ·cm^2 for the DED-LB sample).

3.3.2. Potentiodynamic polarisation curves in a broad potential range

To account for the differences in corrosion resistance between DED-LB and wrought Ti−6Al–4 V samples observed by EIS measurements at OCP (Fig. 12, Table 3), PDP curves were measured in a broad potential region between −150 mV vs. OCP to 6 V vs. Ag/AgCl in HBSS, NaCl and AS.

First, samples were allowed to stabilise for 1.5 h at OCP. The DED-LB sample consistently exhibited more positive OCP values than the wrought sample, indicating that the former was less prone to passivation (Table 4). In HBSS, the OCP for the DED-LB sample was −0.024

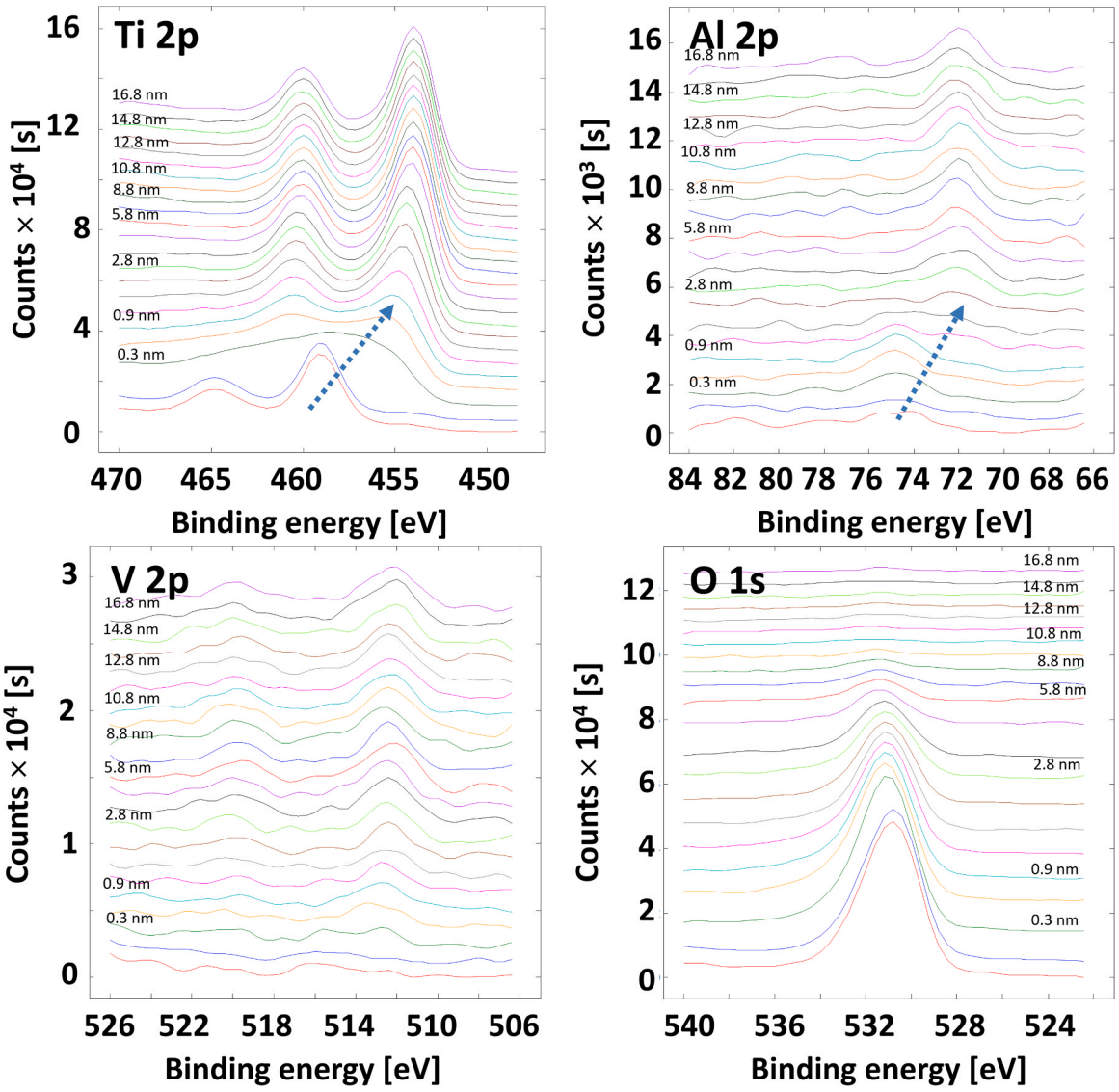

Fig. 11. XPS depth profiles of Ti 2p, Al 2p, V 2p and O 1 s spectra recorded at the chemo-mechanically polished surface of the DED-LB Ti–6Al–4 V sample. The sputtering rate was 1 nm/min. The depth at which spectra were recorded is written in the graphs.

± 0.092 V, more noble than −0.222 ± 0.094 V for the wrought alloy. Similar trends were observed in 0.9 wt% NaCl, where the DED-LB sample maintained an OCP of 0.042 ± 0.032 V compared to −0.313 ± 0.058 V for the wrought sample, and in AS, with values of 0.037 ± 0.035 V and −0.289 ± 0.040 V, respectively.

The PDP curves for both samples, recorded over a broad potential range, illustrate these differences, showing the characteristic trends in corrosion parameters (E_{corr} and j_{corr}) across all tested solutions. PDP curves recorded for the DED-LB consistently demonstrated more positive E_{corr} and comparable or slightly higher j_{corr} relative to the wrought sample (Fig. 14). The E_{corr} and j_{corr} determined from the PDP curves recorded in HBSS, 0.9 wt% NaCl, and AS are summarised in Table 4. For instance, in HBSS, the DED-LB alloy had an E_{corr} of −0.094 ± 0.076 V, significantly more positive than the wrought sample's − 0.319 ± 0.086 V. The j_{corr} values were comparable, at 0.015 ± 0.007 μA·cm^{-2} for the DED-LB and 0.012 ± 0.002 μA·cm^{-2} for the wrought sample.

In 0.9 wt% NaCl, an increased j_{corr} was noted for the DED-LB sample (0.053 ± 0.012 μA· cm^{-2}) compared to the wrought sample (0.014 ± 0.003 μA·cm^{-2}), whose value remained similar as in HBSS. It seems that when aggressive chloride ions are the only components in the solution, they are more aggressive to the oxide layer formed on the DED-LB sample. It has been shown that in simulated physiological solutions containing phosphates and other inorganic salts, such as HBSS, a certain amount of these components (Ca and phosphate) is incorporated in the oxide layer, contributing to its resistance [73]. The DED-LB sample maintained a more positive E_{corr} (−0.074 ± 0.032 V versus −0.336 ± 0.018 V for the wrought sample). Similarly, in AS, the DED-LB alloy exhibited j_{corr} of 0.059 ± 0.034 μA·cm^{-2}, similar to that in 0.9 wt% NaCl and greater than in HBSS. In AS, E_{corr} was somewhat more positive than in NaCl, −0.039 ± 0.066 V. AS contains fewer chloride ions than HBSS, but also sulphide ions and urea. This may have an adverse effect on the oxide layer and affect the corrosion current density [8].

Following the corrosion potential, the passive region is established already at ~0.5 V, followed by the second region of independent current density on potential at ~2.5 V, extending up to 6 V. The current density in the latter region is lower for the DED-LB sample (Fig. 14). These two regions are related to the progressive transformation of Ti-suboxides to TiO_2 and its thickening at higher electrode potentials [7].

The electrochemical response of the samples cut from different positions of the printed wall (left-centre-right, Fig. S1) was checked. PDP curves recorded for samples from different positions overlap, confirming the homogeneous chemical composition of the printed wall (Fig. S6).

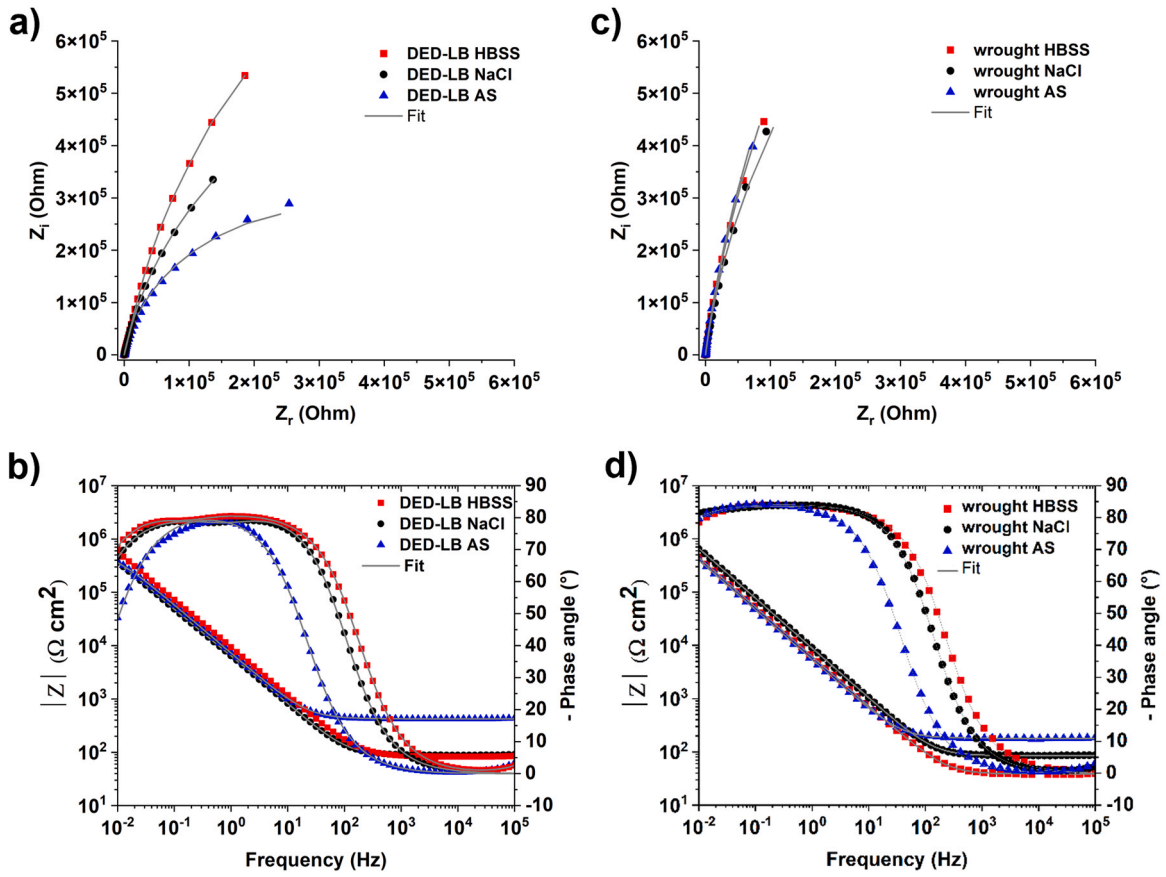

Fig. 12. (a, c) Nyquist plots of real and imaginary components of impedance (Z_i and Z_r) vs. frequency (f) and (b, d) Bode plots of impedance magnitude and phase angle (Θ) vs. f for (a, b) DED-LB and (c, d) wrought Ti–6Al–4 V samples at OCP in Hanks balanced salt solution (HBSS), 0.9 wt% NaCl and artificial saliva solution (AS) at 37 °C after 1.5 h of immersion. Experimental data are presented by symbols and fitted results by solid lines. EIS spectra related to wrought Ti–6Al–4V in NaCl and AS were previously published in [55] and are presented here for comparison.

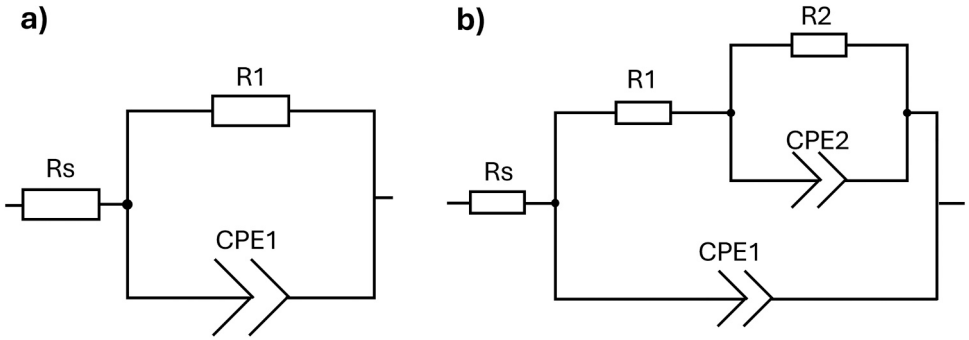

Fig. 13. Equivalent electrical circuit models used for EIS fitting in HBSS, NaCl, and AS solutions. (a) EEC used to fit EIS results for DED-LB Ti–6Al–4 V in AS and wrought Ti–6Al–4V in HBSS, NaCl and AS, and (b) EEC used to fit EIS results for DED-LB Ti–6Al–4 V in HBSS and NaCl.

Table 3
Values of fitted parameters of EIS measurements recorded for wrought and DED-LB Ti–6Al–4V samples in HBSS, 0.9 wt% NaCl and AS solutions (Fig. 13). The fitting was conducted using EECs in Fig. 13. EIS results related to wrought Ti–6Al–4 V in NaCl and AS were previously published in ref. [55] and are presented here for comparison.

Sample / Solution	R_s [Ω·cm²]	R_p [MΩ·cm²]	R_1 [MΩ·cm²]	CPE_1 [μΩ^{-1} s^n cm^{-2}]	n_1	R_2 [MΩ·cm²]	CPE_2 [μΩ^{-1} s^n cm^{-2}]	n_2	χ^2	Θ at 10 mHz [°]
DED-LB / HBSS	83	3.23	0.689	20.0	0.91	2.54	2.0	0.88	0.057	−71
DED-LB / NaCl	88	1.54	0.043	26.5	0.93	1.50	5.6	0.82	0.007	−68
DED-LB / AS	422	0.64	0.642	26.0	0.91	/	/	/	0.034	−49
wrought / HBSS	38	5.70	5.70	29.2	0.93	/	/	/	0.015	−73
wrought / NaCl	85	8.09	8.09	20.0	0.94	/	/	/	0.010	−81
wrought / AS	393	8.80	8.80	24.5	0.94	/	/	/	0.009	−84

Table 4
Electrochemical data for DED-LB and wrought Ti–6Al–4 V samples obtained from potentiodynamic measurements in HBSS, 0.9 wt% NaCl and artificial saliva solution presented in Fig. 14 (OCP open circuit potential, E_{corr} corrosion potential, and j_{corr} corrosion current density).

Sample / Solution	OCP [V]	E_{corr} [V]	j_{corr} [μA cm^{-2}]
DED-LB / HBSS	−0.024 ± 0.092	−0.094 ± 0.076	0.015 ± 0.007
DED-LB / NaCl	0.042 ± 0.032	−0.074 ± 0.032	0.053 ± 0.012
DED-LB / AS	0.037 ± 0.035	−0.039 ± 0.066	0.059 ± 0.034
wrought / HBSS	−0.222 ± 0.094	−0.319 ± 0.086	0.012 ± 0.002
wrought / NaCl	−0.312 ± 0.057	−0.334 ± 0.025	0.014 ± 0.003
wrought / AS	−0.296 ± 0.041	−0.337 ± 0.030	0.015 ± 0.005

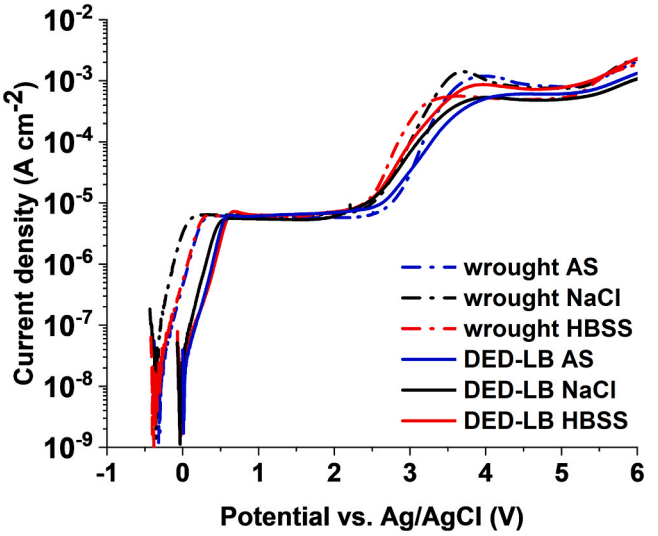

Fig. 14. Potentiodynamic polarisation curves of wrought and DED-LB manufactured titanium samples Ti–6Al–4 V after 1.5 h of immersion in Hanks' balanced salt solution (HBSS), 0.9 wt% NaCl and artificial saliva (AS) at 37 °C. PDP curves related to wrought. PDP curves related to wrought Ti–6Al–4 V in NaCl and AS were previously published in ref. [55] and are presented here for comparison. The scan rate was 1 mV/s.

Summarising, the E_{corr} is consistently more positive for DED-LB samples than for wrought samples for 220 −320 mV. The j_{corr} values span between 0.011 and 0.015 μA· cm^{-2} for wrought samples and are similar for all three solutions. For DED-LB samples, the j_{corr} values are between 0.015 and 0.059 μA· cm^{-2}, greater in NaCl and AS solutions. Generally, DED-LB samples in the broad potential range up to 6 $V_{Ag/AgCl}$ show typical polarisation curves across all three solutions, similar to wrought samples. However, differences observed in EIS measurements at OCP, with DED-LB samples being more prone to dissolution in chloride solution and artificial saliva, were confirmed in a broad potential region.

In the literature reports, SLM [36,38,41–43,74] and EBM [68] Ti–6Al–4 V alloys mainly achieved comparable or slightly worse corrosion resistance than wrought samples in 3.5 wt % NaCl at room temperature [68], artificial saliva at 37 °C [41,42], Kukubo physiological solution at room temperature [36], 0.9 wt% NaCl at 37 °C [43], 0.9 wt% NaCl at pH 4.2 [38] and NaCl and HCl solution [74]. The worse corrosion resistance of AM samples was in the literature reports ascribed to the local inclusions and discontinuities at the sample surface [36], a less dense passive layer [74], less corrosion resistance of the β-phase [42,43], and the non-uniform distribution of alloying elements [68]. Fewer literature reports are available for DED-manufactured alloys. DED-Ti–6Al–4 V showed significantly worse corrosion performance in 15 % NaCl (pH 6.2) than the rolled samples [49], ascribed to α/α' with a low content of β phase. Similarly, susceptibility to localised corrosion was noted for DED Ti–6Al–4 V samples in 3.5 % NaCl [50].

3.3.3. Changes in surface morphology and composition due to polarisation in NaCl and artificial saliva solutions

The electrochemical measurements were further complemented with SEM/EDS analysis of the samples' surface following the polarisation to 6 $V_{Ag/AgCl}$. This condition was chosen to follow the PDP curves in Fig. 14; however, it should be kept in mind that the conditions of such high positive potentials are rather extreme compared to the physiological conditions in a human body and should be regarded more as a mechanistic feature. SEM/EDS analyses for bare wrought and DED-LB Ti–6Al–4 V samples and after polarisation in HBSS, NaCl and AS to 6 $V_{Ag/AgCl}$ are shown in Figs. 15 and 16. The corresponding EDS analyses are given in Tables 5 and 6. Images recorded at smaller magnification (5000 ×) are given in Figs. S7 and S8.

The SEM/EDS analysis of bare wrought and DED-LB Ti–6Al–4 V samples is already detailed in Fig. 6 and is presented again at different magnification herein for comparative purposes with polarised samples. In the wrought sample, site 1 refers to Al-rich α matrix with no vanadium, and site 2 to β-phase grain rich in V (Fig. 15a and b, Table 5). After polarisation to 6 $V_{Ag/AgCl}$ in 0.9 wt% NaCl (Fig. 15c and d, Table 5), several features were observed. The matrix is covered by a more or less thick oxide layer (sites 3 and 4, seen as light grey and dark grey in the CBS image, Fig. 15d). Some V was also detected in the matrix. The Ti content was over 70 wt% and O content was less than 20 wt%. Further, several large grains were pulled out of the structure, obviously related to the β-phase grain (sites 5 and 6). The combination of ICE and CBS images (Fig. 15c and d) shows that the grains are missing, but the sites are filled or bordered with corrosion products, where some Cl and Na were also detected. EDS analysis confirmed that these sites are rich in V and O and lean in Ti.

After polarisation to 6 $V_{Ag/AgCl}$ in artificial saliva (Fig. 15e and f, Table 5), several differences were observed compared to those in 0.9 wt % NaCl. Sites 7 and 8 refer to an oxide-layer matrix with a high Ti content. In addition to O, some phosphorus was also detected. Sites 7 and 8 differ in Ti and O contents, with the latter showing less Ti. Again, some missing grains were filled with abundant corrosion products (sites 9 −11). These sites are strongly enriched in V and O and depleted in Ti. Their morphology suggests that these products grow from the pulled-out β-grains and are related to the dissolution of V-rich sites, resulting in V-oxide. It has been shown that the V is strongly prone to dissolution in simulated body fluids than Ti [8,75]. The formation of the V-oxide products is more pronounced than that of the NaCl solution. The SEM/EDS analysis shows that after polarisation of wrought sample to 6 $V_{Ag/AgCl}$ the surface is subjected to corrosion primarily at the β-phase grains rich in V. The corrosion attack leads to pulled-out grain and formation of V-oxide, especially in artificial saliva, as already noted. However, the surrounding Al-rich α matrix remains covered by an oxide layer and seems to counteract the corrosion of the β phase.

In the DED-LB sample, site 1 refers to Al-rich α matrix with a small V content, and sites 2 and 3 to β-phase grains rich in V (Fig. 16a and b, Table 6). After polarisation to 6 $V_{Ag/AgCl}$ in 0.9 wt% NaCl (Fig. 16c and d, Table 6), abundant changes were observed on the sample surface. Similar to the wrought sample, the Al-rich matrix is covered by a more or less thick oxide layer (sites 4 and 5, seen as light grey and dark in the CBS image, Fig. 16d). This oxide contains 2 −3 wt% of V. Interesting are longitudinal areas bordering the Al-rich matrix (represented by site 6). Here, V and O concentrations were higher (> 4 wt%), and Ti concentrations were reduced. These areas are related to prior β grains (e.g., site 3 in Fig. 16a). It seems that the dissolution started at these sites and then exposed larger areas with higher V concentration (site 7), again leading to stronger dissolution and pulled-out grains (seen in the CBS image in Fig. 16d) and formation of abundant V-oxide, as observed [41]. At these sites, the concentrations of V and O were high, and that of Ti was reduced (Table 6).

After polarisation to 6 $V_{Ag/AgCl}$ in artificial saliva (Fig. 16e and f, Table 6), the corrosion pattern with longitudinally etched prior β grains and formation of V-oxide corrosion products was again more

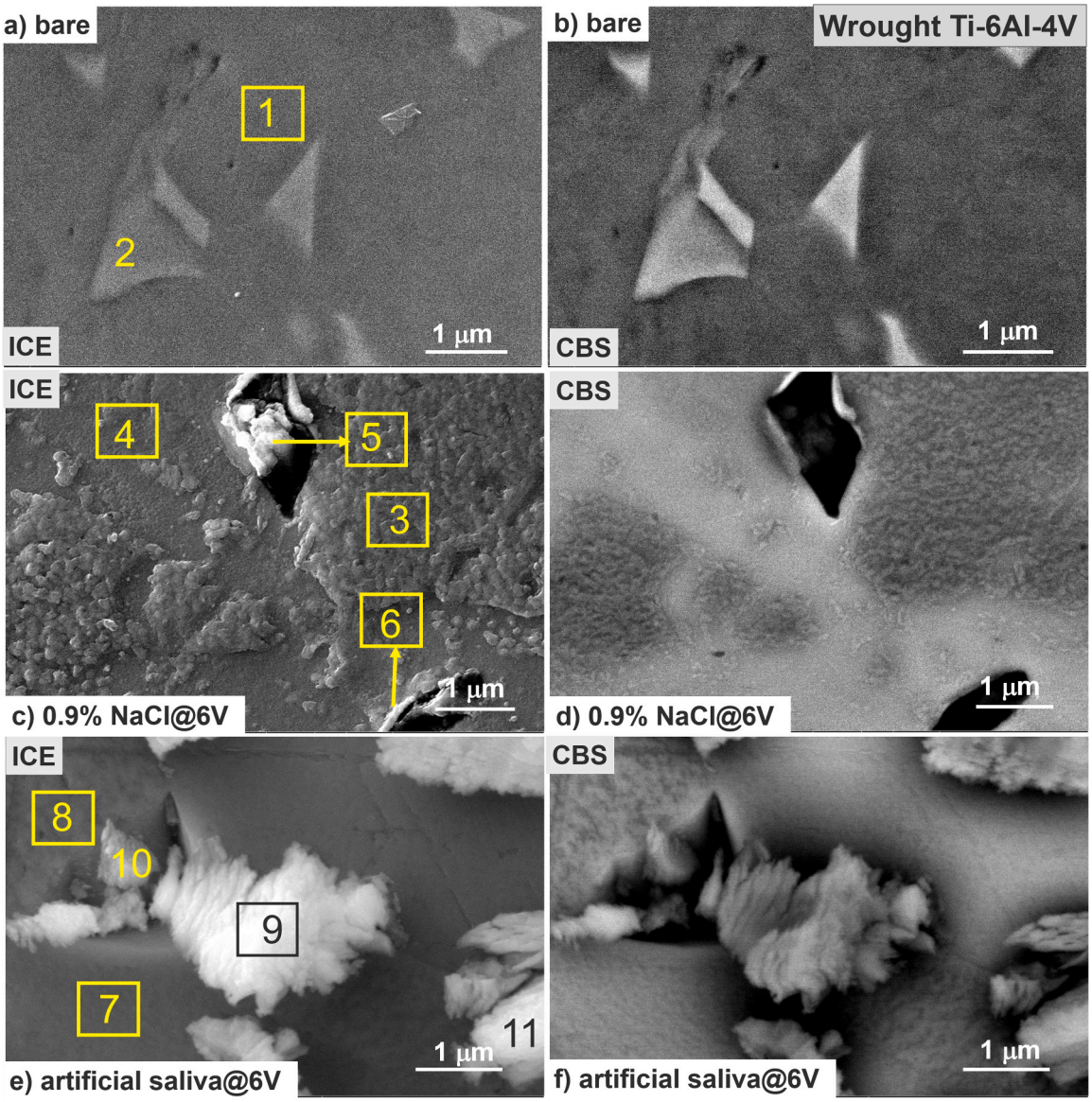

Fig. 15. SEM images of surface morphology of a) bare chemo-mechanically polished wrought Ti–6Al–4 V and after potentiodynamic polarisation to b) 6 $V_{Ag/AgCl}$ in 0.9 wt% NaCl and c) 6 V in artificial saliva (Fig. 14). Numbers denote the sites at which EDS analysis was conducted; the results are given in Table 5. Images were recorded at high magnification (20,000 ×) using ICE (secondary electrons) and CBS (back-scattered electrons) detectors. Images taken at lower magnification (5000 ×) are given in Supplement (Fig. S7).

emphasised than in NaCl solution. The CBS image shows that areas of the thicker oxide layer (darker sites) at the matrix were absent in AS, indicating a thinner oxide layer. In contrast to NaCl, corrosion product contains phosphorus originating from AS.

3.3.4. The effect of polarisation in simulated physiological solutions on the vanadium dissolution

The basic corrosion mechanism can be postulated based on the combined results from OCP, EIS, PDP, and SEM/EDS of wrought and DED-LB Ti–6Al–4 V samples in three simulated physiological solutions. At OCP, both alloys are protected by the predominantly TiO_2 passive layer, which shows minimal deviations in surface potential and assures a homogeneous coverage, as indicated by XPS/SEM/AFM/SKPFM analysis. Both types of Ti–6Al–4 V show exceptional corrosion resistance in simulated physiological solutions in the MΩ·cm^2 range. The analysis of EIS measurements at OCP and corrosion parameters of the PDP curves (E_{corr}, j_{corr} and R_p) show that wrought alloy exhibits excellent corrosion resistance in all three physiological solutions tested, with almost no difference in j_{corr} and R_p values in the range between about 6 and 8 MΩ·cm^2 for HBSS, NaCl and AS. DED-LB alloy also shows very high R_p values in the MΩ·cm^2 range, but smaller than for the wrought sample (between 0.6 and 3 MΩ·cm^2). Also, j_{corr} values, although remaining in the nm·cm^{-2} range, increase 4-fold in NaCl and AS compared to HBSS. These findings underscore the influence of electrolyte composition on the passive film characteristics and confirm the DED-LB alloy's suitability for biomedical applications, particularly in environments that promote passive oxide layer stability, such as HBSS [42,74]. In more aggressive solutions, AS and NaCl, the DED-LB alloy's somewhat worse corrosion resistance can be ascribed to the martensite α/α' microstructure less corrosion resistant than α+ β structure, thinner spontaneously formed oxide layer less capable of preventing the chloride attack and the presence of occasional pores or defects present in the printed samples.

Upon polarisation to 6 $V_{Ag/AgCl}$ the differences in the corrosion mechanism of wrought and DED-LB Ti–6Al–4 V samples in three simulated physiological solutions became evident. For wrought sample, the corrosion process proceeds mainly at the β grains, rich in V. The strong

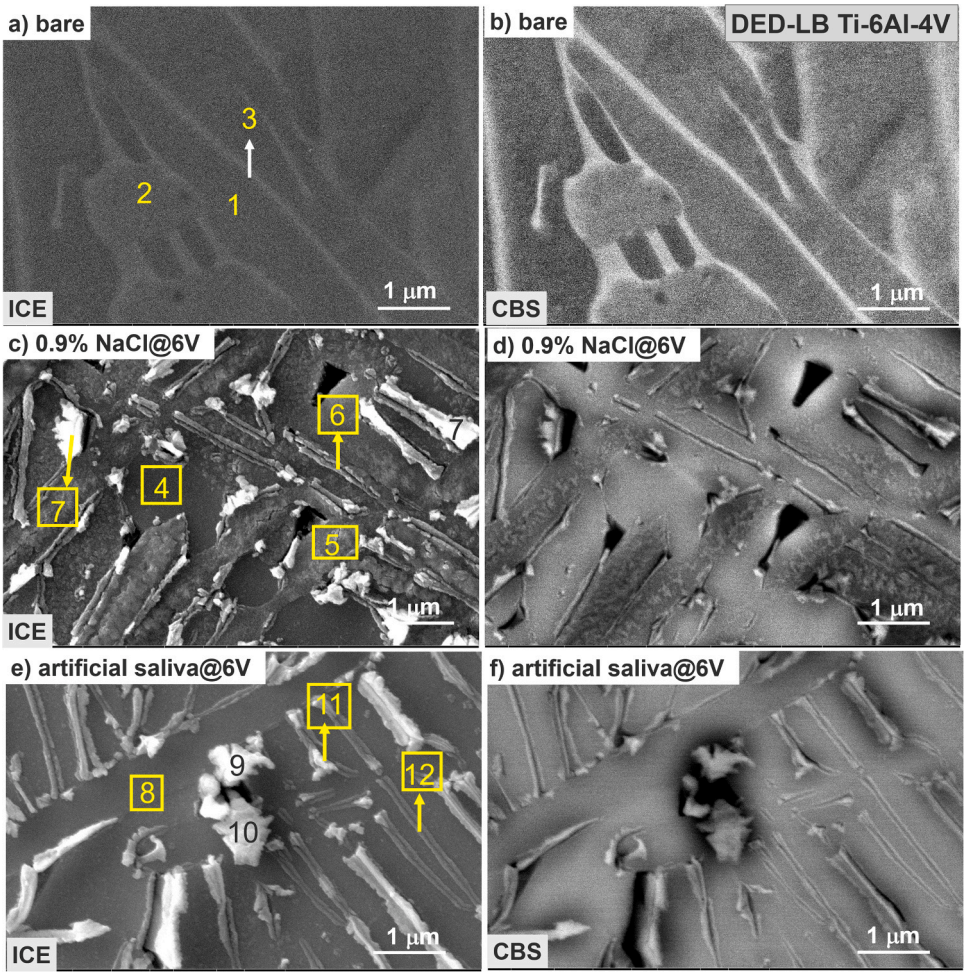

Fig. 16. SEM images of surface morphology of a) bare chemo-mechanically polished wrought Ti–6Al–4 V and after potentiodynamic polarisation to b) 6 $V_{Ag/AgCl}$ in 0.9 wt% NaCl and c) 6 V in artificial saliva (Fig. 14). Numbers denote the sites at which EDS analysis was conducted; the results are given in Table 6. Images were recorded at high magnification (20,000 ×) using ICE (secondary electrons) and CBS (back-scattered electrons) detectors. Images taken at lower magnification (5000 ×) are given in Supplement (Fig. S8).

Table 5
Elemental composition in wt% determined by point EDS analysis at numbered sites in Fig. 15 for the wrought Ti–6Al–4 V sample, which was polarised to 6 $V_{Ag/AgCl}$ in 0.9 wt% NaCl and artificial saliva.

Site	composition (wt%)						
	Ti	Al	V	O	Na	Cl	P
	bare						
1	93.4	6.6	-	-	-	-	-
2	80.8	3.3	15.9	-	-	-	-
polarised to 6 V in 0.9 wt% NaCl							
3	76.3	5.1	2.2	16.4	-	-	-
4	85.0	5.4	2.0	7.6	-	-	-
5	49.5	2.6	12.9	32.8	1.3	0.9	-
6	63.9	3.0	11.3	21.4	0.4	-	-
polarised to 6 V in artificial saliva							
7	87.7	4.4	2.4	5.1	-	-	0.4
8	71.7	4.3	3.2	20.4	-	-	0.4
9	38.2	1.3	10.7	48.1	-	-	1.7
10	54.6	3.1	6.7	34.7	-	-	0.9
11	42.6	2.0	10.6	43.2	-	-	1.6

Table 6
Elemental composition in wt% determined by point EDS analysis at numbered sites in Fig. 16 for the DED-LB Ti–6Al–4 V sample, which was polarised to 6 $V_{Ag/AgCl}$ in 0.9 wt% NaCl and artificial saliva.

Site	composition (wt%)						
	Ti	Al	V	O	Na	Cl	P
	bare						
1	91.5	6.3	2.2	-	-	-	-
2	90.5	6.3	3.2	-	-	-	-
3	85.5	4.8	9.6	-	-	-	-
polarised to 6 V in 0.9 wt% NaCl							
4	80.2	5.3	3.0	11.5	-	-	-
5	70.9	4.6	2.5	22.0	-	-	-
6	75.4	4.8	4.5	15.3	-	-	-
7	62.4	4.2	4.4	29.0	-	-	-
polarised to 6 V in artificial saliva							
8	81.9	5.4	2.3	10.4	-	-	
9	53.6	3.9	4.3	37.2	-	-	1.0
10	60.4	4.1	3.7	30.9	-	-	0.9
11	66.3	4.4	5.1	23.7	-	-	0.5
12	69.8	4.5	4.6	20.6	-	-	0.5

dissolution of V at these sites leads to the formation of V-oxide-rich corrosion products. The surrounding α matrix, however, remains virtually undamaged and predominantly covered by Ti-oxide layer, which also contains some V (presumably originating from the dissolution of the phase). Cyclic polarisation curve shows that the current density decreases upon reversal of the polarisation direction at 6 $V_{Ag/AgCl}$ and does not form a hysteresis, indicating that the layer can repassivate even after such substantial corrosion damage (Fig. S6). The dissolution is stronger in artificial saliva than in NaCl solution.

For the DED-LB sample, vanadium dissolution concentrated along the longitudinal prior β-grains is spread over the whole surface, aligned with the microstructure of the additively manufactured samples (Fig. 6b). Whereas for the wrought sample, isolated β grains are subject to dissolution and then counteracted by the repassivation of the α phase, the dissolution of the longitudinal β grains of the DED-LB sample encroach on a larger part of the α phase, making it difficult for the latter to protect larger areas fully. This process results in the etching of the surface and forming a larger amount of V-oxide-rich corrosion product. As for the wrought alloy, the cyclic polarisation curve shows no hysteresis in the reverse cycle.

4. Conclusions

The comparative analysis between wrought Ti–6Al–4 V and DED-LB Ti–6Al–4 V alloys revealed distinct micro- and macrostructural properties arising from the different thermal conditions of the two processes (Table 7). Optical imaging and SEM/EDS/AFM confirmed that metallurgical Ti–6Al–4 V displays a refined, equiaxed α+ β grain structure with uniform distribution.

- Conversely, DED-LB Ti–6Al–4 V is characterised by a coarser lamellar structure aligned with the heat flow during laser-directed energy deposition. Rapid cooling rates in DED-LB lead to a directional solidification pattern, with a martensitic α' phase, manifested as needle-like lamellar structures surrounded by prior β grains.
- The general chemical composition of DED-LB Ti–6Al–4 V aligns with the wrought alloy, demonstrating that the DED-LB process effectively fabricates Ti–6Al–4 V alloy from powder, maintaining its chemical integrity.
- Microstructural differences induce differences in chemical composition at the local micrometre level. A clear distinction between the wrought and DED-LB samples is the distribution of vanadium. In the wrought sample, V is concentrated predominantly in β-phase grains, reaching about 16 wt%. In the DED-LB sample, V is concentrated in the longitudinal prior β-phase at a smaller content (8 −9 wt%) than in the wrought sample, but it is present also in the matrix phase (2 −3 wt%).
- Wrought Ti–6Al–4 V displays minimal porosity and defect occurrence, contributing to consistent mechanical integrity. The DED-LB samples show rare, occasional pores.
- Despite the differences in microstructure, both alloys exhibit similar polarisation behaviour, reflecting the highly protective corrosion resistance of the TiO_2 passive layer, as shown by polarisation and EIS measurements in Hanks' balanced salt solution, NaCl and artificial saliva. However, minor differences in corrosion resistance were noted. Namely, the polarisation resistance for DED-LB samples ranged between 0.64 and 3.23 MΩ·cm^2 in AS, NaCl and HBSS, respectively; in contrast, the wrought samples achieved greater values between 5.7 and 8.80 MΩ·cm^2. These results indicate that the corrosion protection assured by the DED-LB samples is slightly reduced compared to the wrought samples, especially in NaCl and artificial saliva; in HBSS, the adverse effect of chloride ions is counteracted by phosphate ions.
- Upon polarisation to 6 $V_{Ag/AgCl}$ the differences in the corrosion mechanism of wrought and DED-LB Ti–6Al–4 V samples in three simulated physiological solutions became evident. The strong dissolution of V at the β grains leads to the formation of V-oxide-rich corrosion products. The surrounding α matrix, however, remains virtually undamaged and predominantly covered by Ti-oxide layer. For the DED-LB sample, the dissolution of vanadium from the longitudinal β grains encroach on a larger part of the α matrix, making it difficult for the latter to protect larger areas fully. This process results in the etching of the surface and forming a larger amount of V-oxide-rich corrosion product.

Table 7
Comparison of the metallurgically and additively manufactured Ti–6Al–4 V.

Feature	wrought Ti–6Al–4 V	DED-LB Ti–6Al–4 V
α-phase	Well-defined, equiaxed grains.	Elongated, columnar grains.
β-phase	Grains distributed within α-phase.	Longitudinal areas of prior β grains along the elongated α-phase
Martensitic α' phase	Absent or minimal.	Present, needle-like structures within the α-Ti phase.
Porosity and defects	Minimal, rarely observed.	More common, visible as pores or voids.
Corrosion resistance in simulated body fluids.	Excellent corrosion resistance in all types of physiological solutions.	Very good corrosion resistance, but dependent on the type of physiological solution.
Dissolution mechanism upon high anodic polarisation	Limited to β-phase grains, rich in vanadium.	Spread longitudinally along prior β-phase, rich in vanadium.

- With advancements in process optimisation, DED-LB can expand its applicability to industries requiring intricate designs, such as aerospace, biomedical implants, and automotive manufacturing, as will be addressed in our following study.

CRediT authorship contribution statement

Barbara Kapun: Validation, Investigation, Formal analysis. **Peter Rodič:** Writing – review & editing, Writing – original draft, Formal analysis, Conceptualization. **Anish Nair:** Writing – review & editing, Validation, Investigation. **Denis Sačer:** Writing – review & editing, Validation, Investigation, Formal analysis. **Davorin Kramar:** Writing – review & editing, Validation, Investigation. **Edvard Govekar:** Writing – review & editing, Validation, Investigation, Conceptualization. **Andrej Jeromen:** Writing – review & editing, Validation, Investigation. **Ingrid Milošev:** Writing – review & editing, Writing – original draft, Validation, Methodology, Investigation, Funding acquisition, Conceptualization.

Funding sources

The authors acknowledge the Slovenian Research and Innovation Agency (ARIS) for the funding of the project »Antibacterial alloys: Development by additive 3D manufacturing, characterisation and clinical applications«, acronym BIOAD, https://bioad.ijs.si/ (grant No. J7–4639) and core funding (grants No. P2–0393, No. P1–0134, and No. P2–0241).

Declaration of Competing Interest

The authors declare that they have no known competing financial interests or personal relationships that could have appeared to influence the work reported in this paper.

Acknowledgements

The XPS analysis was conducted at the Department of Surface Engineering of the Jožef Stefan Institute (Prof. Janez Kovač and Tatjana Filipič, MSc). The XRD analysis was conducted at the National Institute of Chemistry, Ljubljana, by Prof. Nataša Zabukovec Logar. The KPFM and AFM topography with AFM LiteScope and BSE signal by CBS detector, all in SEM Versa (FEI), were performed by NenoVision (Veronika Hegrová and Tomáš Kostovčík). The authors acknowledge using SEM/EDS equipment at the Center for Electron Microscopy and Microanalysis (CEMM) of the Jožef Stefan Institute and Nanocenter Center of Excellence for Nanoscience and Nanotechnology.

Appendix A. Supporting information

Supplementary data associated with this article can be found in the online version at doi:10.1016/j.jallcom.2025.181280.

Data availability statement

The data supporting this study's findings are available on request from the corresponding author.

References

[1] P. Yadav, K.K. Saxena, Effect of heat-treatment on microstructure and mechanical properties of Ti alloys: an overview, Mater. Today Proc. 26 (2020) 2546–2557, https://doi.org/10.1016/j.matpr.2020.02.541.

[2] P. Bocchetta, L.-Y. Chen, J.D.C. Tardelli, A.C. dos Reis, F. Almeraya-Calderón, P. Leo, Passive layers and corrosion resistance of biomedical Ti-6Al-4V and β-Ti alloys, Coatings 11 (2021) 487, https://doi.org/10.3390/coatings11050487.

[3] M. Geetha, A.K. Singh, R. Asokamani, A.K. Gogia, Ti based biomaterials, the ultimate choice for orthopaedic implants – a review, Prog. Mater. Sci. 54 (2009) 397–425, https://doi.org/10.1016/j.pmatsci.2008.06.004.

[4] G. Sander, J. Tan, P. Balan, O. Gharbi, D.R. Feenstra, L. Singer, S. Thomas, R. G. Kelly, J.R. Scully, N. Birbilis, Corrosion of additively manufactured alloys: a review, Corrosion 74 (2018) 1318–1350, https://doi.org/10.5006/2926.

[5] N. Lin, D. Li, J. Zou, R. Xie, Z. Wang, B. Tang, Surface texture-based surface treatments on Ti6Al4V titanium alloys for tribological and biological applications: a mini review, Materials 11 (2018) 487, https://doi.org/10.3390/ma11040487.

[6] H.J. Haydar, J. Al-Deen, A.K. AbidAli, A.A. Mahmoud, Improved performance of Ti6Al4V alloy in biomedical applications - review, J. Phys. Conf. Ser. 1973 (2021) 012146, https://doi.org/10.1088/1742-6596/1973/1/012146.

[7] I. Milošev, M. Metikoš-Huković, H.-H. Strehblow, Passive film on orthopaedic TiAlV alloy formed in physiological solution investigated by X-ray photoelectron spectroscopy, Biomaterials 21 (2000) 2103–2113, https://doi.org/10.1016/S0142-9612(00)00145-9.

[8] I. Milošev, B. Kapun, V.S. Šelih, The effect of fluoride ions on the corrosion behaviour of Ti metal, and Ti–6Al–7Nb and Ti–6Al–4V alloys in artificial saliva, Acta Chim. Slov. 60 (2013) 543–555.

[9] M. Popa, J.M. Calderon Moreno, C. Vasilescu, S.I. Drob, E.I. Neacsu, A. Coer, J. Hmeljak, G. Žerjav, I. Milošev, Structural analysis, electrochemical behavior, and biocompatibility of novel quaternary titanium alloy with near β Structure, Metall. Mater. Trans. A 45 (2014) 3130–3143, https://doi.org/10.1007/s11661-014-2254-9.

[10] X.P. Ren, H.Q. Li, H. Guo, F.L. Shen, C.X. Qin, E.T. Zhao, X.Y. Fang, A comparative study on mechanical properties of Ti–6Al–4V alloy processed by additive manufacturing vs. traditional processing, Mater. Sci. Eng. A 817 (2021) 141384, https://doi.org/10.1016/j.msea.2021.141384.

[11] F. Ji, R. Liu, Z. Wang, J. Liu, L. Guan, Z. Liu, Y. Bai, The mechanical coupling effect of α and β phases in Ti6Al4V alloy undergoing laser shock peening: a molecular dynamics study, Mater. Sci. Eng. A 915 (2024) 147208, https://doi.org/10.1016/j.msea.2024.147208.

[12] S. Liu, Y.C. Shin, Additive manufacturing of Ti6Al4V alloy: a review, Mater. Des. 164 (2019) 107552, https://doi.org/10.1016/j.matdes.2018.107552.

[13] D. Herzog, V. Seyda, E. Wycisk, C. Emmelmann, Additive manufacturing of metals, Acta Mater. 117 (2016) 371–392, https://doi.org/10.1016/j.actamat.2016.07.019.

[14] L. Thijs, F. Verhaeghe, T. Craeghs, J.V. Humbeeck, J.-P. Kruth, A study of the microstructural evolution during selective laser melting of Ti–6Al–4V, Acta Mater. 58 (2010) 3303–3312, https://doi.org/10.1016/j.actamat.2010.02.004.

[15] J.S. Keist, T.A. Palmer, Role of geometry on properties of additively manufactured Ti-6Al-4V structures fabricated using laser based directed energy deposition, Mater. Des. 106 (2016) 482–494, https://doi.org/10.1016/j.matdes.2016.05.045.

[16] D. Mah, M.H. Pelletier, V. Lovric, W.R. Walsh, Corrosion of 3D-printed orthopaedic implant materials, Ann. Biomed. Eng. 47 (2019) 162–173, https://doi.org/10.1007/s10439-018-02111-1.

[17] S.M. Kelly, S.L. Kampe, Microstructural evolution in laser-deposited multilayer Ti-6Al-4V builds: Part I. Microstructural characterization, Metall. Mater. Trans. A 35 (2004) 1861–1867, https://doi.org/10.1007/s11661-004-0094-8.

[18] Y. Wu, J. Liu, L. Kang, J. Tian, X. Zhang, J. Hu, Y. Huang, F. Liu, H. Wang, Z. Wu, An overview of 3D printed metal implants in orthopedic applications: present and future perspectives, Heliyon 9 (2023) e17718, https://doi.org/10.1016/j.heliyon.2023.e17718.

[19] Y. Watanabe, S. Yamada, T. Chiba, H. Sato, S. Miura, K. Abe, T. Kato, Microstructure and strength of Ti-6Al-4V samples additively manufactured with TiC heterogeneous nucleation site particles, Materials 16 (2023) 5974, https://doi.org/10.3390/ma16175974.

[20] F. Frölich, L. Bechtloff, B.M. Scheuring, A.L. Heuer, F. Wittemann, L. Kärger, W. V. Liebig, Evaluation of mechanical properties characterization of additively manufactured components, Prog. Addit. Manuf. 10 (2024) 1217–1229, https://doi.org/10.1007/s40964-024-00700-2.

[21] P. Chandramohan, S. Bhero, B.A. Obadele, P.A. Olubambi, Laser additive manufactured Ti–6Al–4V alloy: tribology and corrosion studies, Int. J. Adv. Manuf. Technol. 92 (2017) 3051–3061, https://doi.org/10.1007/s00170-017-0410-2.

[22] M. Shaikh, F. Kahwash, Z. Lu, M. Alkhreisat, A. Mohammad, I. Shyha, Revolutionising orthopaedic implants—a comprehensive review on metal 3D printing with materials, design strategies, manufacturing technologies, and post-process machining advancements, Int. J. Adv. Manuf. Technol. 134 (2024) 1043–1076, https://doi.org/10.1007/s00170-024-14218-y.

[23] J. Tjandra, E. Alabort, D. Barba, S. Pedrazzini, Corrosion, fatigue and wear of additively manufactured Ti alloys for orthopaedic implants, Mater. Sci. Technol. 39 (2023) 2951–2965, https://doi.org/10.1080/02670836.2023.2230417.

[24] J. Liu, K. Zhang, Y. Yang, H. Wang, Y. Zhu, A. Huang, Grain boundary α-phase precipitation and coarsening: Comparing selective laser melted and conventional manufactured Ti6Al4V, Scripta Mater 207 (2022) 114261, https://doi.org/10.1016/j.scriptamat.2021.114261.

[25] M. Peters, J. Hemptenmacher, J. Kumpfert, C. Leyens, Structure and properties of titanium and titanium alloys. Titanium and Titanium Alloys: Fundamentals and Applications, John Wiley & Sons, Ltd, 2003, pp. 1–36, https://doi.org/10.1002/3527602119.ch1.

[26] T. DebRoy, H.L. Wei, J.S. Zuback, T. Mukherjee, J.W. Elmer, J.O. Milewski, A. M. Beese, A. Wilson-Heid, A. De, W. Zhang, Additive manufacturing of metallic components – process, structure and properties, Prog. Mater. Sci. 92 (2018) 112–224, https://doi.org/10.1016/j.pmatsci.2017.10.001.

[27] D. Svetlizky, M. Das, B. Zheng, A.L. Vyatskikh, S. Bose, A. Bandyopadhyay, J. M. Schoenung, E.J. Lavernia, N. Eliaz, Directed energy deposition (DED) additive manufacturing: physical characteristics, defects, challenges and applications, Mater. Today 49 (2021) 271–295, https://doi.org/10.1016/j.mattod.2021.03.020.

[28] D. Svetlizky, B. Zheng, A. Vyatskikh, M. Das, S. Bose, A. Bandyopadhyay, J. M. Schoenung, E.J. Lavernia, N. Eliaz, Laser-based directed energy deposition (DED-LB) of advanced materials, Mater. Sci. Eng. A 840 (2022) 142967, https://doi.org/10.1016/j.msea.2022.142967.

[29] P.A. Kobryn, S.L. Semiatin, Microstructure and texture evolution during solidification processing of Ti–6Al–4V, J. Mater. Process. Technol. 135 (2003) 330–339, https://doi.org/10.1016/S0924-0136(02)00865-8.

[30] G. Soundarapandiyan, C.L.A. Leung, C. Johnston, B. Chen, R.H.U. Khan, P. McNutt, A. Bhatt, R.C. Atwood, P.D. Lee, M.E. Fitzpatrick, *In situ* monitoring the effects of Ti6Al4V powder oxidation during laser powder bed fusion additive manufacturing, Int. J. Mach. Tools Manuf. 190 (2023) 104049, https://doi.org/10.1016/j.ijmachtools.2023.104049.

[31] G. Piscopo, E. Atzeni, A. Saboori, A. Salmi, An overview of the process mechanisms in the laser powder energy deposition, Appl. Sci. 13 (2023) 117, https://doi.org/10.3390/app13010117.

[32] Y. Zhang, S. Shen, H. Li, Y. Hu, Review of in situ and real-time monitoring of metal additive manufacturing based on image processing, Int. J. Adv. Manuf. Technol. 123 (2022) 1–20, https://doi.org/10.1007/s00170-022-10178-3.

[33] J. Mi, Y. Zhang, H. Li, S. Shen, Y. Yang, C. Song, X. Zhou, Y. Duan, J. Lu, H. Mai, In-situ monitoring laser based directed energy deposition process with deep convolutional neural network, J. Intell. Manuf. 34 (2023) 683–693, https://doi.org/10.1007/s10845-021-01820-0.

[34] N. Bastola, M.P. Jahan, N. Rangasamy, C.S. Rakurty, A review of the residual stress generation in metal additive manufacturing: analysis of cause, measurement, effects, and prevention, Micromachines 14 (2023) 1480, https://doi.org/10.3390/mi14071480.

[35] B. Wysocki, P. Maj, R. Sitek, J. Buhagiar, K.J. Kurzydłowski, W. Święszkowski, Laser and electron beam additive manufacturing methods of fabricating titanium bone implants, Appl. Sci. 7 (2017) 657, https://doi.org/10.3390/app7070657.

[36] Y.B. Bozkurt, Y.S. Kavasoğlu, B. Atik, H. Kovacı, Y. Uzun, A. Çelik, Comparison study of corrosion behavior for chitosan coated Ti6Al4V alloy produced by selective laser melting and forging, Prog. Org. Coat. 182 (2023) 107655, https://doi.org/10.1016/j.porgcoat.2023.107655.

[37] Z. Cai, H. Nakajima, M. Woldu, A. Berglund, M. Bergman, T. Okabe, In vitro corrosion resistance of titanium made using different fabrication methods, Biomaterials 20 (1999) 183–190, https://doi.org/10.1016/S0142-9612(98)00160-4.

[38] J. Fojt, M. Fousova, E. Jablonska, L. Joska, V. Hybasek, E. Pruchova, D. Vojtech, T. Ruml, Corrosion behaviour and cell interaction of Ti-6Al-4V alloy prepared by two techniques of 3D printing, Mater. Sci. Eng. C 93 (2018) 911–920, https://doi.org/10.1016/j.msec.2018.08.066.

[39] J. Fojt, V. Hybášek, Z. Kačenka, E. Průchová, Influence of surface finishing on corrosion behaviour of 3D printed TiAlV alloy, Metals 10 (2020) 1547, https://doi.org/10.3390/met10111547.

[40] K. Karolewska, B. Ligaj, Comparison Analysis of Titanium Alloy Ti6Al4V Produced by Metallurgical and 3D Printing Method, AIP Conf. Proc. 2077 (2019) 020025. ⟨https://doi.org/10.1063/1.5091886⟩.

[41] M.B. Leban, T. Kosec, M. Finšgar, Corrosion characterization and ion release in SLM-manufactured and wrought Ti6Al4V alloy in an oral environment, Corros. Sci. 209 (2022) 110716, https://doi.org/10.1016/j.corsci.2022.110716.

[42] M. Bajt Leban, T. Kosec, M. Finšgar, The corrosion resistance of dental Ti6Al4V with differing microstructures in oral environments, J. Mater. Res. Technol. 27 (2023) 1982–1995, https://doi.org/10.1016/j.jmrt.2023.10.082.

[43] F. Toptan, A.C. Alves, Ó. Carvalho, F. Bartolomeu, A.M.P. Pinto, F. Silva, G. Miranda, Corrosion and tribocorrosion behaviour of Ti6Al4V produced by selective laser melting and hot pressing in comparison with the commercial alloy, J. Mater. Process. Technol. 266 (2019) 239–245, https://doi.org/10.1016/j.jmatprotec.2018.11.008.

[44] H. Wang, B. Zhao, C. Liu, C. Wang, X. Tan, M. Hu, A comparison of biocompatibility of a titanium alloy fabricated by electron beam melting and selective laser melting, PLOS ONE 11 (2016) e0158513, https://doi.org/10.1371/journal.pone.0158513.

[45] L. Weiss, P. Acquier, L. Germain, E. Fleury, Microtexture of Ti6Al4V obtained by direct energy deposition (DED) process, in: Proc. 13th World Conf. Titan., John Wiley & Sons, Ltd, 2016: pp. 1305–1310. ⟨https://doi.org/10.1002/9781119296126.ch221⟩.
[46] S.Q. Wu, Y.J. Lu, Y.L. Gan, T.T. Huang, C.Q. Zhao, J.J. Lin, S. Guo, J.X. Lin, Microstructural evolution and microhardness of a selective-laser-melted Ti–6Al–4V alloy after post heat treatments, J. Alloy. Compd. 672 (2016) 643–652, https://doi.org/10.1016/j.jallcom.2016.02.183.
[47] H. Zhang, W. Qin, C. Man, H. Cui, D. Kong, Z. Cui, X. Wang, C. Dong, Effect of heat treatment on microstructure and corrosion behavior of Ti6Al4V fabricated by laser beam powder bed fusion, Corros. Sci. 209 (2022) 110789, https://doi.org/10.1016/j.corsci.2022.110789.
[48] A. Leon, G. Katarivas Levy, T. Ron, A. Shirizly, E. Aghion, The effect of strain rate on stress corrosion performance of Ti6Al4V alloy produced by additive manufacturing process, J. Mater. Res. Technol. 9 (2020) 4097–4105, https://doi.org/10.1016/j.jmrt.2020.02.035.
[49] S.A. Shalnova, M.O. Gushchina, D.A. Strekalovskaya, E.L. Alekseeva, O.G. Klimova-Korsmik, Electrochemical properties of the heat-treated Ti-6Al-4V alloy manufactured by direct energy deposition, J. Alloy. Compd. 899 (2022) 163226, https://doi.org/10.1016/j.jallcom.2021.163226.
[50] H. Oh, J.G. Kim, J. Lee, S. Kim, Environment-assisted fatigue crack propagation (EAFCP) behavior of Ti64 Alloy fabricated by direct energy deposition (DED) process, Metall. Mater. Trans. A 53 (2022) 3604–3614, https://doi.org/10.1007/s11661-022-06765-4.
[51] M. Hierro-Oliva, A.M. Gallardo-Moreno, M.L. González-Martín, XPS analysis of Ti6Al4V oxidation under UHV conditions, Metall. Mater. Trans. A 45 (2014) 6285–6290, https://doi.org/10.1007/s11661-014-2570-0.
[52] M.F. López, J.A. Jiménez, A. Gutiérrez, XPS characterization of surface modified titanium alloys for use as biomaterials, Vacuum 85 (2011) 1076–1079, https://doi.org/10.1016/j.vacuum.2011.03.006.
[53] D.N.G. Krishna, J. Philip, Review on surface-characterization applications of X-ray photoelectron spectroscopy (XPS): recent developments and challenges, Appl. Surf. Sci. Adv. 12 (2022) 100332, https://doi.org/10.1016/j.apsadv.2022.100332.
[54] Standard practice for exposure of metals and alloys by alternate immersion in neutral 3.5% sodium chloride solution, ⟨https://www.astm.org/g0044-21.html⟩ (accessed October 7, 2024).
[55] I. Milošev, D. Sačer, B. Kapun, P. Rodič, The effect of metallographic preparation on the surface characteristics and corrosion behaviour of Ti-6Al-4V alloy in simulated physiological solutions, J. Electrochem. Soc. 171 (2024) 111503, https://doi.org/10.1149/1945-7111/ad8e89.
[56] E. Govekar, A. Jeromen, A. Kuznetsov, G. Levy, M. Fujishima, Study of an annular laser beam based axially-fed powder cladding process, CIRP Ann. 67 (2018) 241–244, https://doi.org/10.1016/j.cirp.2018.04.082.
[57] H.D. Nguyen, A. Pramanik, A.K. Basak, Y. Dong, C. Prakash, S. Debnath, S. Shankar, I.S. Jawahir, S. Dixit, D. Buddhi, A critical review on additive manufacturing of Ti-6Al-4V alloy: microstructure and mechanical properties, J. Mater. Res. Technol. 18 (2022) 4641–4661, https://doi.org/10.1016/j.jmrt.2022.04.055.
[58] Standard practice for microetching metals and alloys, ⟨https://www.astm.org/e0407-07r15e01.html⟩ (accessed October 10, 2024).
[59] K.V. Yang, G.R. de Looze, V. Nguyen, R.S. Wilson, Directed-energy deposition of Ti-6Al-4V alloy using fresh and recycled feedstock powders under reactive atmosphere, Addit. Manuf. 58 (2022) 103043, https://doi.org/10.1016/j.addma.2022.103043.
[60] B.C. Muddle J.F. Nie Encyclopedia of Materials: Science and Technology Second Edition 2001 5189 5193.https://doi.org/10.1016/B0-08-043152-6/00901-3.
[61] M. Wang, Y. Wu, S. Lu, T. Chen, Y. Zhao, H. Chen, Z. Tang, Fabrication and characterization of selective laser melting printed Ti–6Al–4V alloys subjected to heat treatment for customized implants design, Prog. Nat. Sci. Mater. Int. 26 (2016) 671–677, https://doi.org/10.1016/j.pnsc.2016.12.006.
[62] R.W. Cahn, P. Haasen, E.J. Kramer, D.F. Williams, Materials science and technology: a comprehensive treatment. Medical and Dental Materials, 14 ed., Wiley-VCH, Weinheim, 1992.
[63] H.-J. Yi, J.-W. Kim, Y.-L. Kim, S. Shin, Effects of cooling rate on the microstructure and tensile properties of wire-arc additive manufactured Ti–6Al–4V alloy, Met. Mater. Int. 26 (2020) 1235–1246, https://doi.org/10.1007/s12540-019-00563-1.
[64] H. Jaber, J. Kónya, K. Kulcsár, T. Kovács, Effects of annealing and solution treatments on the microstructure and mechanical properties of Ti6Al4V manufactured by selective laser melting, Materials 15 (2022) 1978, https://doi.org/10.3390/ma15051978.
[65] K. Grujić, A review of thermal spectral imaging methods for monitoring high-temperature molten material streams, Sensors 23 (2023) 1130, https://doi.org/10.3390/s23031130.
[66] J. He, D. Li, W. Jiang, L. Ke, G. Qin, Y. Ye, Q. Qin, D. Qiu, The martensitic transformation and mechanical properties of Ti6Al4V prepared via selective laser melting, Materials 12 (2019) 321, https://doi.org/10.3390/ma12020321.
[67] K. Bower, S. Murray, A. Reinhart, A. Nieto, Corrosion resistance of selective laser melted Ti–6Al–4V alloy in salt fog environment, Results Mater. 8 (2020) 100122, https://doi.org/10.1016/j.rinma.2020.100122.
[68] V. Dehnavi, J.D. Henderson, C. Dharmendra, B.S. Amirkhiz, D.W. Shoesmith, J. J. Noël, M. Mohammadi, Corrosion behaviour of electron beam melted Ti6Al4V: effects of microstructural variation, J. Electrochem. Soc. 167 (2020) 131505, https://doi.org/10.1149/1945-7111/abb9d1.
[69] Y. Zhang, J. Li, S. Che, Z. Yang, Y. Tian, Chemical leveling mechanism and oxide film properties of additively manufactured Ti–6Al–4V alloy, J. Mater. Sci. 54 (2019) 13753–13766, https://doi.org/10.1007/s10853-019-03855-4.
[70] NIST X-ray Photoelectron Spectroscopy (XPS) Database, Version 3.5, (2000). ⟨https://srdata.nist.gov/xps⟩/ (accessed May 6, 2018).
[71] I. Milošev, T. Kosec, H.-H. Strehblow, XPS and EIS study of the passive film formed on orthopaedic Ti–6Al–7Nb alloy in Hank's physiological solution, Electrochim. Acta 53 (2008) 3547–3558, https://doi.org/10.1016/j.electacta.2007.12.041.
[72] I. Milošev, G. Žerjav, J.M. Calderon Moreno, M. Popa, Electrochemical properties, chemical composition and thickness of passive film formed on novel Ti–20Nb–10Zr–5Ta alloy, Electrochim. Acta 99 (2013) 176–189, https://doi.org/10.1016/j.electacta.2013.03.086.
[73] I. Milošev, The effect of biomolecules on the behaviour of CoCrMo alloy in various simulated physiological solutions, Electrochim. Acta 78 (2012) 259–273, https://doi.org/10.1016/j.electacta.2012.05.146.
[74] C. Bai, P. Li, T. Gang, J. Li, M. Wei, Y. Huang, L. Chen, Influence of processing technology on electrochemical corrosion behavior of Ti-6Al-4V alloys, Corrosion 77 (2021) 402–412, https://doi.org/10.5006/3490.
[75] M. Metikoš-Huković, A. Kwokal, J. Piljac, The influence of niobium and vanadium on passivity of titanium-based implants in physiological solution, Biomaterials 24 (2003) 3765–3775, https://doi.org/10.1016/S0142-9612(03)00252-7.